Exploring the ability of the variable-resolution CESM to simulate cryospheric-hydrological variables in High Mountain Asia

René R. Wijngaard[1,*], Adam R. Herrington[2], William H. Lipscomb[2], Gunter R. Leguy[2], and Soon-Il An[1,3]

[1]Irreversible Climate Change Research Center, Yonsei University, Seoul, South Korea
[2]Climate and Global Dynamics Laboratory, National Center for Atmospheric Research, Boulder CO, USA
[3]Climate Theory Lab, Department of Atmospheric Sciences, Yonsei University, Seoul, South Korea
[*]Now at: Institute for Marine and Atmospheric Research Utrecht, Utrecht University, Utrecht, the Netherlands

Correspondence to: Soon-Il An (sian@yonsei.ac.kr) and René R. Wijngaard (r.r.wijngaard.uu@gmail.com)

Abstract. Earth System Models (ESMs) can help to improve the understanding of climate-induced cryospheric-hydrological impacts in complex mountain regions, such as High Mountain Asia (HMA). Coarse ESM grids, however, have difficulties in representing cryospheric-hydrological processes that vary over short distances in complex mountainous environments. Variable-resolution (VR) ESMs can~~ould~~ help through targeted grid refinement to overcome these limitations. This study investigates the ability of the VR-Community Earth System Model (VR-CESM) to simulate cryospheric-hydrological variables such as glacier surface mass balance (SMB) over HMA. To this end, a new VR grid is generated with regional grid refinement up to 7 km over HMA. Two coupled atmosphere-land simulations are run for the period 1979–1998. The second simulation is performed with an updated glacier-cover dataset and includes snow and glacier model modifications. ~~To evaluate the outcomes,~~ Comparisons are made to gridded outputs derived from a globally uniform 1° CESM grid, observation-, reanalysis-, and satellite-based datasets, and a glacier model forced by a regional climate model (RCM). ~~In general,~~ Climatological biases are generally reduced compared to the coarse-resolution CESM grid, but glacier SMB is too negative relative to observation-based glaciological and geodetic mass balances as well as RCM-forced glacier model output. In the second simulation, the SMB is improved but is still underestimated due to cloud-cover and temperature biases, missing model physics, and incomplete land-atmosphere coupling. The outcomes suggest that VR-CESM could be a useful tool to simulate cryospheric-hydrological variables and to study climate change in mountainous environments, but further developments are needed to better simulate the SMB of mountain glaciers.

1 Introduction

High Mountain Asia (HMA) encompasses the South and Central Asian Mountain ranges (e.g., the Himalayas, Karakoram, Pamir, and Tien Shan) and the highlands of the Tibetan Plateau. The region, also known as the “Asian Water Tower”, hosts the largest reserves of snow and glacier ice outside the polar regions and provides essential water resources for millions of

people living in the region and surrounding lowlands (Yao et al., 2012; Immerzeel et al., 2020). By modulating the release of meltwater into rivers, the glaciers and snow reserves can sustain seasonal water availability and are therefore important contributors to the water supply for irrigation, drinking water, hydropower, industry, and ecosystem services (Nie et al., 2021; Lutz et al., 2022).

In recent decades, ongoing climate change has reduced snow volumes and driven the widespread retreat of glaciers worldwide (Hock et al., 2019). Similar trends have been observed in HMA over the last few decades, although the response to climate change is regionally dependent~~differs per region~~. Differences are linked, in part, to spatial and seasonal contrasts in precipitation patterns that are associated with the complex interplay between topography, the westerlies, and the Indian and East Asian monsoon systems (Yao et al., 2012). Westerlies drive precipitation during winter/spring in the western part of HMA, whereas the Indian and East Asian monsoon systems are dominant to the east and south and deliver large amounts of precipitation during the monsoon season (June-September) (Wijngaard et al., 2017; Lutz et al., 2019). In response to climate change, rising temperatures and a weakened summer monsoon have led to negative snowfall trends and reduced snow water equivalent (SWE) in most regions under the influence of the monsoon systems (Yao et al., 2012; Smith and Bookhagen, 2018). Also, many HMA glaciers have lost mass since the end of the Little Ice Age (~1300–1850) with accelerated mass losses over the last few decades (Brun et al., 2017; Zemp et al., 2019; Shean et al., 2020). This is in contrast to the western part of HMA (i.e., Pamir, Kunlun Shan, Tien Shan, Karakoram) where westerlies have strengthened over the last few decades (Cannon et al., 2015), possibly leading to increased winter snowfall and SWE (Cannon et al., 2015; Smith and Bookhagen, 2018). Furthermore, glaciers in a few regions (e.g., Karakoram, western Kunlun Shan, and eastern Pamir) have stayed in balance or gained mass in recent decades (Brun et al., 2017).

In the future, it is projected that glaciers in HMA will continue to lose mass and that snow cover and volume will decline further (Viste and Sorteberg, 2015; Kraaijenbrink et al., 2017). These changes will impact seasonal water availability, negatively affecting downstream populations and infrastructure (Nie et al., 2021; Li et al., 2022)~~(Nie et al., 2021)~~. Furthermore, the risk for natural hazards, such as glacial lake outburst floods (GLOFs) and riverine floods, might increase. Downstream climate in East and South Asia might be affected, and global mean sea level will rise (Frey et al., 2010; Wijngaard et al., 2017; Marzeion et al., 2020; Li et al., 2022)~~(Frey et al., 2010; Wijngaard et al., 2017; Marzeion et al., 2020)~~. For this reason, we need to better understand the potential impacts of glacier retreat and changing snow regimes, which requires more accurate estimates of glacier surface mass balance (SMB) and snow conditions (e.g., snow cover and snow depth).

To derive the present and future state of glaciers and snow conditions in HMA, a variety of modelling approaches have been used, ranging from glacier models (Kraaijenbrink et al., 2017; Marzeion et al., 2020) to regional climate models (RCMs). RCMs have been applied with one-way or two-way coupling to glacier models (Mölg and Kaser, 2011; Collier et al., 2013; Bonekamp et al., 2019; Rahimi et al., 2019; de Kok et al., 2020). Glacier evolution models are usually forced by statistically downscaled global climate models (GCMs) or by datasets based on observations or reanalysis. These models are computationally efficient, which enables them to be applied at fine~~high~~ horizontal resolution (varying from ~100 m to 50

km) or acrossfor many glaciers over a long period of time (Marzeion et al., 2020). One limitation, however, is that glacier models use one-way coupling with the atmosphere without including feedbacks between the glacier or land surface and the atmosphere (Collier et al., 2013). Also, uncertainties are introduced due to the scale mismatch between coarse-gridded climate models and datasets, and small-scale mountain glaciers embedded in complex topography (Mölg and Kaser, 2011; Collier et al., 2013). To overcome these limitations and better understand the atmospheric drivers and their feedbacks with glaciers and snow, RCMs can be suitable tools, since they can be applied at high spatio-temporal resolution with horizontal grid spacing as fine as 1 km (Bonekamp et al., 2019). RCMs can better resolve the complex topography, while also providing detailed meteorological fields to compare with in-situ observations and providinggiving more information about land-atmosphere interactions (van Kampenhout et al., 2019). RCMs, however, need to be forced by GCMs or global reanalysis products, which disables a two-way interaction between the region of interest and the global domain.

GCMs can be more appropriate modelling tools since they allow two-way interactions, avoiding inconsistencies between RCMs and GCMs in terms of dynamics and physics parameterizations (Huang et al., 2016). Until now, GCMs have generally not been considered as suitable for simulating SMB or snow conditions due to insufficient spatio-temporal resolution, model biases, and unresolved snow/ice physical processes, such as meltwater refreezing and snow-albedo feedbacks (Vizcaino, 2014). Recent improvements, however, have increased the suitability of some GCMs or Earth System Models (ESMs) for simulating SMB and snow conditions. These improvements include: 1) multilayer snow models with parameterizations for snow densification, refreezing, and albedo (Flanner and Zender, 2005; van Kampenhout et al., 2017), 2) elevation tiles or classes to account for subgrid variability and downscaling SMB with altitude (Lipscomb et al., 2013; Shannon et al., 2019), and 3) surface-energy-balance schemes to simulate snow and ice melt (Vizcaíno et al., 2013). With these improvements, GCMs and ESMs such as the Community Earth System Model (CESM) have simulated increasingly realistic SMB over the Greenland and Antarctic Ice Sheets (Vizcaíno et al., 2013; Lenaerts et al., 2016; Sellevold et al., 2019; van Kampenhout et al., 2020). This is not the case, however, for the SMB of glaciers in mountainous regions, such as HMA, which require high-resolution grids to capture complex and highly variable topography. This requires large computational resources that are often not available, and thus the application of GCMs or ESMs in mountainous regions has been limited.

Variable-resolution CESM (VR-CESM; Lauritzen et al., 2018) is a potential alternative for applications in complex mountainous terrains. VR-CESM is a hybrid between regional and global climate models, applying regional grid refinement to the atmosphere over a region of interest within a coarse-gridded global domain (Rhoades et al., 2016). In this way, a high-resolution grid can be applied regionally without a prohibitive computational cost for the global model. For example, Huang et al. (2016) conducted Atmospheric Model Intercomparison Project (AMIP) simulations with VR-CESM over the western USA at refined spatial resolution of 0.25° and 0.125° and reduced the computational cost by factors of 10 and 25, respectively, compared to globally uniform high-resolution grids. VR-CESM has been used to study the impacts of regional refinement on, for instance, global circulation and climatology (Gettelman et al., 2018), and the sensitivity of underlying physics to changing model resolution (Gettelman et al., 2018; Herrington and Reed, 2020). VR-CESM has also been applied

over mountainous areas. In the western USA and the Chilean Andes, it has been used with regional refinements up to 7 km to simulate regional climate and snowpack (Huang et al., 2016; Rhoades et al., 2016, 2018; Bambach et al., 2021; Xu et al., 2021)~~(Huang et al., 2016; Rhoades et al., 2016; Bambach et al., 2021; Xu et al., 2021)~~. Also, over the Tibetan Plateau, South Asia, and East Asia, it has been applied to study the regional climate and snow characteristics (Rahimi et al., 2019; Xu et al., 2021). The application of VR-CESM to simulate glacier SMB has been limited, thus far, to the Greenland Ice Sheet (van Kampenhout et al., 2019; Herrington et al., 2022).

The main aim of this study is to investigate the ability of the VR-CESM v2.1 to simulate SMB and snow conditions over High Mountain Asia. We also evaluate the simulation of other climatic and cryospheric-hydrological variables, such as precipitation and temperature. To this end, a VR grid is generated with horizontally refined grid spacings of 7 km (0.0625°) over HMA. The VR grid is used to run two transient model simulations covering a 20-year period, 1979–1998. The second simulation uses an updated glacier-cover dataset, snow and glacier model modifications, and revised cloud tunings. We compare the model results with gridded outputs derived from a globally uniform 1° CESM run, reanalysis- and satellite-based datasets, and a glacier model forced by the Weather Research and Forecasting (WRF) model. Compared to previous VR-CESM studies conducted for HMA (Rahimi et al., 2019), this study has several novelties. The VR-grid includes one more factor of refinement compared to Rahimi et al. (2019), who refined the grid to 14 km over the Tibetan Plateau and southern parts of HMA (i.e., excluding the Tien Shan). Also, this study is the first ESM application that investigates the simulation of mountain glacier SMB in High Mountain Asia, which is important for understanding present and future impacts of glacier changes on freshwater availability.

This paper is organized as follows. Section 2 highlights the methods and data and briefly describes the model. Section 3 presents and discusses the main outcomes, including their uncertainties and limitations, which will inform future model development. Section 4 gives conclusions.

2. Data and Methods

2.1 CESM Overview

We use the Community Earth System Model version 2.1 (CESM2; Danabasoglu et al., 2020), a global Earth system modelling framework consisting of several components (including atmosphere, ocean, ocean waves, land surface, river transport, sea ice, and land ice) that can be run in partially or fully coupled mode. With partial coupling, the active components are replaced by external data or stub components. In this study, we apply CESM in a partially coupled mode with active prognostic atmosphere and land surface components and prescribed monthly sea ice and surface temperature (i.e., replacing the active ocean and sea ice components). This configuration follows the AMIP protocol (Gates et al., 1999; Hurrell et al., 2008).

The atmosphere component of CESM2 is the Community Atmosphere Model version 6 (CAM6) with a spectral-element dynamical core enabling VR capabilities (CAM6-SE) and a dry-mass vertical coordinate with 32 vertical levels (Zarzycki et

al., 2014; Lauritzen et al., 2018; Gettelman et al., 2019a). CAM6 physics parameterizations include the Beljaars orographic drag parameterization scheme (Beljaars et al., 2004); a shallow convection, turbulence, and cloud macrophysics scheme (CLUBB; Bogenschutz et al., 2013); a deep convection scheme (Zhang and McFarlane, 1995); a cloud microphysics scheme with prognostic treatment of precipitation (MG2; Gettelman and Morrison, 2015); and a modified modal aerosol module (MAM4; Liu et al., 2016). More detailed information about CAM6-SE can be found in Lauritzen et al. (2018) and Gettelman et al. (2019a).

The land surface component is the Community Land Model version 5 (CLM5; Lawrence et al., 2019), which is applied with satellite phenology (CLM5-SP). CLM5 simulates the surface energy balance, hydrology, biogeochemical cycles, and their interactions with the atmosphere. Compared to previous CLM versions (e.g., Oleson et al., 2013), CLM5 includes several new and updated parametrizations, e.g., for snow, glaciers, and surface characterization (Lawrence et al., 2019). CLM5 has a multilayer snow model with up to 12 layers of snow. By default, the maximum allowed snow depth (H_{max}) is 10 m water equivalent (w.e.), allowing for meltwater refreezing and firn formation. The snow model includes modifications for wind- and temperature-dependent fresh snow density and snow compaction (van Kampenhout et al., 2017). A snowpack radiative heating model (SNICAR) simulates snow albedo and two-way radiative transfer in each snow layer based on effective snow grain size, incoming solar radiation, and aerosol deposition (Flanner and Zender, 2005; Flanner et al., 2007).

CLM grid cells can be represented by five different land units (vegetated, urban, lakes, crops, and glaciers) that can be subdivided into columns and patches. Glacier land units contain multiple independent columns for elevation classes (ECs) to account for large topographic gradients over glaciers. This scheme is used to downscale several atmospheric variables required to calculate the surface energy balance (SEB) and surface mass balance (SMB) in each EC (Lipscomb et al., 2013; Sellevold et al., 2019). Among the atmospheric variables, near-surface (2m) temperature and (optionally) downwelling longwave radiation are downscaled from the mean CLM grid cell elevation to the EC elevation based on uniform environmental lapse rates of 6 K km^{-1} and 32 W m^{-2} km^{-1}, respectively (Lipscomb et al., 2013; Van Tricht et al., 2016). The downscaled longwave radiation in each EC is bounded by 0.5–1.5 times the grid cell mean value and is normalized to conserve the grid cell mean (Van Tricht et al., 2016). Other atmospheric variables, such as specific humidity, are downscaled by assuming a constant relative humidity with altitude (Lipscomb et al., 2013). In this study, we use 36 ECs instead of the default 10 ECs to better resolve the glacier elevation distribution over High Mountain Asia. The 36 ECs are also applied over the Greenland and Antarctic glacier regions (glacier regions in CLM where EC downscaling is applied by default). There are 35 ECs at intervals of 200 m ranging from 0 m to 7000 m, and an additional EC representing glaciers above 7000 m. To each EC, we assign a weight based on the glacier area in that elevation range relative to the total glacier area in the grid cell. Weights are derived from a high-resolution topography dataset (Wijngaard et al., 2023; also see Supplement Section S1). ECs with zero weight are considered “virtual” and do not contribute to the CLM grid cell mean that is coupled to CAM, but they do compute an SEB and SMB for diagnostic purposes.

CLM calculates the SEB using

$$MHF = SW_{net} + LW_{net} + SHF + LHF + GHF \quad (1)$$

where MHF is the melt heat flux, SW_{net} is the net solar radiation, LW_{net} is the net longwave radiation, SHF is the sensible heat flux, LHF is the latent heat flux, and GHF is the conductive or ground heat flux, all with units of W m^{-2}. All terms are defined as positive downward (from the atmosphere toward the surface), except for GHF, which is defined as positive upward (from the subsurface to the surface).

The SMB in CLM is defined as the total mass flux resulting from capping excess snow, minus the total ice melt and sublimation (van Kampenhout et al., 2020). When the snowpack is thicker than the maximum allowed depth, the excess snow is transformed into ice, resulting in a positive SMB. When snowpack is absent, the SMB can become negative due to bare ice that is melting or sublimating. In all other cases, the SMB is equal to 0. The CLM definition of the SMB differs from the glaciological definition in that it does not include variations in snow depth. The SMB corresponding to the glaciological definition can be computed as (Lenaerts et al., 2019; van Kampenhout et al., 2019, 2020):

$$SMB = PR - RU - SU_{sfc} - SU_{ds} - ER_{ds} \quad (2)$$

where PR is the total rainfall and snowfall, RU is the runoff, SU_{sfc} is the sublimation/evaporation at the surface, and SU_{ds} and ER_{ds} are the sublimation and erosion as a result of drifting snow, all with units of m w.e. yr^{-1}. Since CESM does not include the last two terms, these terms are assumed here to be zero.

The SMB and temperature simulated in CLM can be coupled to the Community Ice Sheet Model (CISM; Lipscomb et al., 2019), the CESM component that simulates the dynamics of glaciers and ice sheets (Muntjewerf et al., 2021). In this study, however, CISM is not used to simulate HMA glaciers, since CISM grids for HMA and other mountain glacier regions are still under development. To enable future testing of CISM with CLM forcing for HMA, the EC-level output from this study has been saved.

2.2 HMA-VR Grid and Performance.

Variable-resolution CESM uses a high-connectivity VR spectral element grid (hereafter HMA_VR7) that is generated by the SQuadGen software package (Ullrich, 2014). SQuadGen offers two refinement types, LOWCONN and CUBIT (Guba et al., 2014). While LOWCONN grids have better numerical stability, the refinement is constructed from large 2x2 element building blocks, making it difficult to generate grids with irregular refinement boundaries. The HMA_VR7 grid (Figure 1a) has horizontally refined grid spacings of ~7 km (0.0625°) over the entire HMA domain, with its boundaries determined by the trace of the landscape surrounding the Tibetan Plateau and adjacent HMA mountain ranges, such as the Himalayas. Because of the irregular refinement boundaries, the HMA_VR7 grid is constructed using the CUBIT method.

Three transition grids with horizontal grid spacings of ~14 km (0.125°), ~28 km (0.25°), and ~55 km (0.5°) serve as a buffer between the HMA domain and the global 1° (~111 km) domain. The 0.5° grid extends from the Black Sea in the west to the Yellow Sea in the east, and from the Indian Peninsula in the south to Siberia in the north. To ensure a smooth transition between varying grid resolutions as well as numerical stability, the buffer zone spans up to five spectral elements, with spring dynamics used to smooth the grid-transition zones and to create nearly orthogonal angles between elements (Guba et al., 2014). The HMA_VR7 grid contains 226,964 horizontal grid points, about 4.7 times more than on a globally uniform 1° SE grid (48,600 grid points).

To find a balance between computational cost and numerical stability, the CAM-SE time-stepping performance of the HMA_VR7 grid was tested in an Aquaplanet environment, a simplified environment that assumes the Earth's surface to be covered by oceans only (Zarzycki et al., 2014). We achieved stability with time steps of 225s and 18.75s for CAM physics and dynamics, respectively, which are 8 and 16 times smaller than the CAM physics (1800s) and dynamics (300s) time steps on a globally uniform 1° SE grid. Hyperviscosity coefficients that prevent numerical artifacts and instability are scaled according to the dimensions of a grid element (Guba et al., 2014). For each halving of the grid resolution, the hyperviscosity coefficients decrease by one order of magnitude (Zarzycki et al., 2014). The VR-CESM simulations were performed on the NCAR's supercomputing facility Cheyenne. With a computational cost of about 90,000 hours per simulated year, the HMA_VR7 grid is about 5% cheaper than a globally uniform 0.25° SE grid (777,600 grid points), which costs about 95,000 hours per simulated year, and about 35 times more expensive than a globally unform 1° SE grid, which costs about 2,500 hours per simulated year. Using 1584–2520 processors (44–70 nodes), the throughput of the HMA_VR7 grid is about 0.3–0.7 simulated years per wall-clock day.

The spectral-element dynamical core used by CESM is currently based on the hydrostatic approximation; non-hydrostatic vertical acceleration terms are neglected, which are important for the representation of deep convection, gravity waves, and flow over topography (Jeevanjee, 2017; Liu et al., 2022). Conventionally, the horizontal scales at which non-hydrostatic terms become important are assumed to be O(10 km), the vertical scale of the troposphere (e.g., Wedi and Smolarkiewicz, 2009). In our 7 km simulations, the smallest resolved scales are between 4 to 6 times the grid spacing (Skamarock et al., 2014; Lauritzen et al., 2018), or between 28 km and 42 km, which suggests that the hydrostatic approximation is appropriate. However, the more recently published studies of Yang et al. (2017) and Liu et al. (2022) have shown that non-hydrostatic terms are important at grid spacings up to 25 km, particularly in its representation of tropical convective systems. Due to the inherent difficulty in testing the null hypothesis (Liu et al., 2022), and that only two studies the authors are aware of have categorically rejected the null hypothesis, we do not believe this is grounds to conclude whether it is appropriate or not to use a 7 km regionally refined grid in combination with a hydrostatic model. Nonetheless, Rhoades et al. (2018) have successfully shown the ability of the hydrostatic VR-CESM to simulate mountainous climate with a 7 km regionally refined grid over the mountain ranges of western USA.

2.3. Topography & Land Surface

The topography of the HMA_VR7 grid was interpolated from the 30-arcsec (~1 km) Global Multi-resolution Terrain Elevation Data (GMTED2010; Danielson and Gesch, 2011) of the United States Geological Survey (USGS) using an updated version of the NCAR Topo software package (Lauritzen et al., 2015). The updated software package includes ridge finding and internal smoothing algorithms to improve the accuracy of high-resolution topography. Figure 2 shows a snapshot of the topography over western HMA (the Karakoram and upper Indus Basin, 32°–37°N; 72°–78°E) for the globally uniform 1° and 0.25° SE CESM grids (hereafter NE30 and NE120, respectively, where NE stands for the number of elements in each coordinate direction on a panel (Lauritzen et al., 2018)) and for the HMA_VR7 grid and GMTED2010. Compared to NE30 and NE120, the HMA_VR7 topography represents the detailed topography of this region more accurately. Over HMA, the maximum altitude increases from 5170 m and 5684 m for NE30 and NE120, respectively, to 6228~~7~~ m for HMA_VR7. These maxima are observed in the northeastern, northwestern, and southeastern HMA subregions (Figure 1b), respectively (Table 1).

The land surface characteristics of the HMA_VR7 grid are partly transient and partly constant. The distribution of plant functional types (PFTs) is transient; time series of land use changes are derived and interpolated from the Land-Use Harmonization (LUH2) time series (Hurtt et al., 2020), which covers the period 1850–2015 and describes annual land-use changes based on the History Database of Global Environment (HYDE version 3.2; Goldewijk et al., 2017). Other land surface classes, such as glaciers and lakes, are assumed constant using the distributions of the year 2000 by default.

2.4 VR-CESM Simulations Setup

We performed two transient model simulations covering a 20-year period, 1979–1998, using the HMA_VR7 grid. Both simulations use several model modifications, including a new glacier region over HMA with a 36-EC scheme in CLM. The new glacier region makes it possible to simulate SMB in multiple (including virtual) ECs in HMA, while retaining the computationally cheaper default behavior of one EC per grid cell in other mountain glacier regions. The HMA glacier region covers a domain between 55°E and 110°E and between 20° N and 50°N.

For the first simulation (hereafter HMA_VR7a), the model is spun up for 1 year. The maximum allowed snow depth (H_{max}) is reduced to 1 m w.e. (the default value in CESM1) under the assumption that a 1-year spin-up is not sufficient to reach H_{max}=10 m w.e. Other CLM settings follow the CESM2 defaults, including a bare-ice albedo of 0.5 (0.3) for the visible (near-infrared) wavebands, the application of longwave downscaling, and rain-snow repartitioning using temperature thresholds of -2°C (0°C) for snow and 0°C (+2°C) for rain over glaciated (non-glaciated) land units. The rain-snow repartitioning is based on downscaled temperature. It uses a linear ramp that assumes precipitation to fall as snow (rain) when the temperature is below (above) the lower (upper) temperature threshold, and as a mix of rain and snow when the temperature is between the two thresholds.

For the second simulation (hereafter HMA_VR7b), the model is initialized with a snow depth of 2.5 m w.e. over glaciated land units, followed by a CAM spin-up of 10 years and a CLM spin-up of 50 years. For the CAM spin-up, CESM is run according to the AMIP protocol, keeping the solar and external forcing, surface emissions, ozone and volcanic aerosols fixed to the 1979 level. The coupler output of this spin-up is used to initialize CLM which is run in a standalone mode and sub-cycles over a 10-year period (i.e., the length of coupler output) for 50 years. A period of 50 years is sufficient to equilibrate the terrestrial system components, such as snowpack. The outputs of the atmospheric and land spin-up are then used to initialize the transient simulation. For HMA_VR7b, we made several model changes to reduce biases compared to HMA_VR7a. These changes include

- An increase in H_{max} from 1 m w.e. to 5 m w.e. to increase the refreezing capacity
- An increase in bare ice albedo to 0.6 (0.4) for visible (near-infrared) wave bands (i.e., the default values in CESM1) to reduce the ice melt.
- Modified rain-snow repartitioning temperature thresholds to 0°C for snow and +4°C for rain over all land units, consistent with observed rain-snow temperature thresholds in HMA (Jennings et al., 2018).
- No downscaling of downward longwave radiation
- Tunings of cloud cover and sea ice, including the MG3 cloud microphysics scheme (Gettelman et al., 2019b). This is an update of the MG2 scheme that includes the effects of graupel or hail. The tunings also include:
    - An increase in the strength of the pressure damping (*CLUBB C11b*) for the third moment of vertical velocity in the large skewness regime from 0.35 to 0.4, to increase low-level cloudiness.
    - An increase in the microphysical auto-conversion size threshold for ice to snow (*micro_mg_dcs*) from 500 x 10^{-6} to 1000 x 10^{-6} m.
    - An increase in snow grain radius (*r_snw*) from 1.25 to 1.5 standard deviations and a decrease in snow melt onset temperature (*dt_melt*) from 1.5 to 1.0°C to tune shortwave radiation and albedo over sea-ice.
- An updated CLM glacier-cover dataset, which is described in more detail in Section S1 of the Supplement.

The differences between HMA_VR7a and HMA_VR7b are also listed in Table 2~~1~~.

2.5 Reference Data

To evaluate the HMA VR simulations, we compare the gridded outputs with outputs from an NE30 CESM run that covers the same 20-year period (1979–1998). We use the following (re)analysis, observation-based, and satellite-derived products, and WRF-based output:

1. The ERA5 reanalysis (Hersbach et al., 2020) is used to evaluate geopotential height and air temperature over the period 1979–1998. ERA5 is available at a spatial resolution of 0.25° x 0.25°, at monthly intervals, and at 37 pressure levels.

2. The WFDEI dataset (Weedon et al., 2014) is used to evaluate 2m temperature, rainfall, and snowfall for 1979–1998. WFDEI stands for Watch Forcing Data methodology applied to ERA-Interim. The dataset has a spatial resolution of 0.5° x 0.5° and uses ERA-Interim output that is corrected for elevation using environmental lapse rates (i.e., for temperature). The data are bias-corrected using gridded observations from datasets developed by the Climate Research Unit (CRU) or the Global Precipitation Climatology Centre (GPCC). In this study we used the WFDEI datasets that are bias-corrected based on GPCC and are available on monthly intervals.
3. Northern Hemisphere (NH) snow-cover extent from the National Snow and Ice Data Center (NSIDC) (Brodzik and Armstrong, 2013) is used to evaluate snow cover for 1979–1998. The NSIDC snow-cover data are available on a 25 x 25 km EASE 2.0 grid at weekly intervals. To enable evaluation of monthly model output, the weekly NSIDC snow-cover data are converted to monthly intervals.
4. The High Asia Refined analysis version 2 (HAR v2; Wang et al., 2021) is used to evaluate snow depth. HARv2 is based on Weather Research and Forecasting (WRF) simulations that are dynamically downscaled with ERA5 and is available on a 10 x 10 km grid at monthly intervals. The snow depth in HARv2 is corrected with snow depth from the Japanese 55-year reanalysis (Kobayashi et al., 2015), which has shown good performance compared to other global reanalysis datasets in simulating snow depth (Orsolini et al., 2019)~~(Orsolini et al., 2019)~~. Since HARv2 data is not available for 1979, we only evaluate the model output for the period 1980–1998.
5. The Japanese 55-year reanalysis (JRA55; Kobayashi et al., 2015) is used to evaluate ~~snow depth and~~ surface-energy-balance components, including all-sky shortwave and longwave surface radiation fluxes as well as latent, sensible, and ground heat fluxes for 1979–1998. JRA55 is available on a T319 Gaussian grid at monthly intervals. ~~and has shown good performance compared to other global reanalysis datasets in simulating snow depth (Orsolini et al., 2019).~~
~~5.~~6. The CERES Energy Balanced and Filled (EBAF) dataset (Loeb et al., 2018; Kato et al., 2018) is used to evaluate shortwave cloud forcing and all-sky shortwave and longwave surface radiation fluxes for 1979–1998. The dataset is available on a 1° x 1° grid at monthly intervals. To evaluate the model output over a similar period (20 years), we use CERES EBAF data covering the period 2001–2020.
~~6.~~7. Glacier SMB is evaluated for 1979–1998 based on two data sources:
    - Area-weighted specific mass change rates derived from glaciological and geodetical observations (Zemp et al., 2019). The observation-based mass change rates are regional estimates based on the RGI regions Central Asia, South Asia West, and South Asia East.
    - Gridded 1° x 1° SMB outputs from a glacier mass balance gradient model forced by temperature and precipitation fields from the Weather Research and Forecasting (WRF) model (de Kok et al., 2020). The gridded SMB outputs are not available for 1979 and only cover the period 1980–1998.

To allow a uniform comparison among the different CESM grids and the (re)analysis and satellite-based datasets, the CESM output and reference data (e.g., WFDEI, NSIDC~~MODIS~~, HARv2, JRA55, CERES-EBAF, and ERA5) are regridded to a 1° finite-volume grid, unless noted otherwise.

3 Results and Discussion

3.1 Northern Hemisphere Atmosphere

Before evaluating the model's ability to simulate cryospheric-hydrological variables such as the glacier SMB, we evaluate its ability to simulate the Northern Hemisphere atmosphere. To this end, we compare geopotential height and air temperature variables simulated by the different CESM grids, using ERA5 output as a reference. Figure 3 shows the lower tropospheric (500–1000 hPa) eddy geopotential thickness in winter and the upper tropospheric (500–200 hPa) mean temperature in summer (The surface of the Tibetan Plateau lies at about 500 hPa). The lower tropospheric eddy geopotential thickness in the left panels of Figure 3 shows the model's ability to simulate stationary wave patterns. The eddy thickness simulated by the NE30 and HMA VR configurations shows many similarities with the ERA5 output, along with some small differences. Both the CESM output and ERA5 output have a stationary wave pattern over the Northern Hemisphere with two negative eddy thickness centers over Siberia and Canada, and two positive eddy thickness centers over the North Pacific and the North Atlantic. The negative eddy centers have a similar shape and magnitude, whereas the positive centers are similar in shape with small differences in magnitude. NE30 is more similar to ERA5 over the North Pacific, whereas the HMA VR configurations are more similar to ERA5 over the North Atlantic.

The upper tropospheric summer temperature biases (relative to ERA5) can help to understand the effects of atmospheric biases on temperature-sensitive surface variables such as ice melt and snow melt. However, atmospheric biases do not necessarily need to correspond with surface temperature biases as we will show in Section 3.3. Compared to ERA5, NE30 shows an elongated warm anomaly over the midlatitudes with the largest warm bias (about +2 K) over Mongolia and northern China. The HMA VR configurations show a similar pattern but with a larger warm bias (about +3K), which is likely related to its higher horizontal resolution. This is a known issue in GCMs and ESMs, particularly at midlatitudes (Roeckner et al., 2006; Herrington and Reed, 2020). One explanation is that increasing horizontal resolution leads to larger resolved vertical velocities and increased condensational heating. This heating, computed in the macrophysics routine of CLUBB, especially raises upper tropospheric temperature at midlatitudes (Herrington and Reed, 2020).

3.2 Cloud Forcing

Figure 4 shows the model's annual mean shortwave cloud radiative forcing (SWCF) biases relative to the CERES-EBAF product. SWCF quantifies the impact of clouds on incident shortwave and is computed as the difference between all-sky and clear-sky shortwave radiative fluxes at the top of the atmosphere. NE30 shows biases typical of CESM2, with positive biases

near the marine stratocumulus decks off the coast of the southwestern U.S. The HMA_VR7a simulation has larger biases than NE30, with more positive biases almost everywhere in the Northern Hemisphere, indicating thinner clouds. This reduction in cloud thickness is primarily due to the smaller physics timestep in the HMA configurations. HMA_VR7b was tuned to remove this sensitivity to physics timestep, resulting in a SWCF bias that looks more similar to the NE30 run (Figure 4b). However, the positive SWCF biases over HMA remain in HMA_VR7b.

Figure 5 shows the summer mean SWCF, which contributes to summer melting. The clouds over the Himalayan front range are too expansive in NE30 compared to CERES-EBAF, spanning 100s of km in the north-south direction. The HMA VR configurations instead produce a narrow SWCF feature over the front range that is more similar to observations (Figure 5a). However, the clouds have mostly disappeared from the northern half of the Tibetan Plateau compared to the NE30 control and CERES-EBAF, as also shown in the annual mean plots in Figure 4. Our cloud tunings in HMA_VR7b are therefore unable to restore clouds locally over the Tibetan Plateau. The VR model's inability to produce realistic mean cloud states inside and outside the refined region is a major limitation of the variable-resolution method (Rauscher et al., 2013).

The bottom panel of Figure 5 shows the summer mean precipitation rates over HMA in the models and the WFDEI validation product. NE30 does not capture the intensity and location of the summer precipitation patterns, in particular over the west coast of India and the eastern side of the Himalayas, extending southward to the eastern coasts of Bangladesh and Burma. In contrast, the HMA VR configurations improve the intensity and location of these features, indicating more realistic monsoonal rainfall.

To explore the causes of the cloud and precipitation changes in the HMA VR runs, Figure 6 shows latitude-height transects averaged over the longitude band 80˚-100˚. The monsoonal circulation in the NE30 run has two centers, a broad region of ascent in the southern HMA region, primarily over the Indian Ocean, and a narrower region of ascent over the front range of the Himalayas (Figure 6d). These ascent centers are collocated with condensational heating from CLUBB (Figure 6g), which sustains the monsoonal circulation. In the HMA VR runs, the ascending center associated with the front range is displaced south, merging with the southern ascent center and manifesting as a single, broad region of ascent (Figures 6e-f). This new circulation is more intense than the NE30 circulation, as shown by a broad region of anomalous condensational heating upwind of the front range (Figures 6h-i) and coinciding with the larger mean precipitation rates in Figure 5.

The anomalous ascent on the south side of the mountains is balanced by anomalous descent on the north side of the plateau (Figures 6e-f). This anomalous descent likely explains the increased temperatures (Figures 6k-l), reduced humidity (Figures 6n-o), and reduced cloudiness (Figures 6q-r) on the north side of the plateau, as these are all consistent with a subsiding environment. While the warming and drying patterns are largely the result of greater vertical velocities due to the enhanced spatial resolution in the HMA VR runs, the shorter physics timestep also contributes to this warming and drying (not shown)~~, which is a common response to reducing the physics timestep (Williamson, 2008; Herrington et al., 2022).~~

3.3 Surface Temperature & Precipitation

Whereas the summer tropospheric temperature over HMA rises with increasing horizontal resolution, the near-surface (2-m) temperature falls. Figure 7 shows the ~~absolute~~ 2-m temperature differences and pattern correlations between the NE30 and HMA VR simulations and the observation/reanalysis-based WFDEI for each season. The ~~absolute~~ differences are shown over four HMA subregions (Figure 1b), and the pattern correlations for the domain 20°-50°N, 65°-105°E. During summer (JJA), NE30 has a warm temperature bias (relative to WFDEI) up to ~2.5°C (here and hereafter, numbers in brackets referring to a bias represent the median bias) over all HMA subregions. This bias decreases with increasing resolution. For HMA_VR7, the JJA warm bias is present only in northern HMA (up to ~2.5°C), whereas southern HMA has a cold bias relative to WFDEI (up to ~2°C). During winter (DJF), spring (MAM) and autumn (SON), cold biases are present over SW-HMA (the region including the Karakoram and Hindu Kush Mountain ranges), growing larger (up to ~8°C) with increasing resolution. Over other HMA subregions, cold biases are also present, but are smaller (up to ~2°C). The cold temperature biases could partly be a result of uncertainties in WFDEI. Since WFDEI is bias-corrected using gridded observations of GPCC, the accuracy of the data relies on the availability of meteorological measurements that are scarce in High Mountain Asia, especially at higher altitude and in the more remote domains of HMA. The lack of measurements could result in temperature overestimates and precipitation underestimates (Lalande et al., 2021; Gu et al., 2012; Palazzi et al., 2015; Immerzeel et al., 2015), which can to some extent explain the cold temperature biases and, as we will show later, the wet precipitation biases that are visible in the NE30 and HMA VR simulation outputs.

The contrary temperature response between the atmosphere (increasing temperature with finer resolution) and land surface (decreasing temperature with finer resolution) can be explained by a combination of better resolved topography and multiple elevation classes for the fine grids. Whereas the NE30 runs have a single EC, the VR runs have 36 ECs for HMA glaciers. With multiple ECs, the atmospheric temperature received from CAM is downscaled with altitude over glaciated land units, which can lower the grid cell mean temperature in highly glaciated regions where glaciers lie above the grid cell mean elevation. The bias difference between NE30 and HMA_VR7 is especially prominent in SW-HMA, the most glaciated subregion. The pattern correlations between WFDEI and CESM as shown in Figure 7b are above 0.95, with the highest correlations in JJA and for HMA_VR7b. This suggests that CESM is able to simulate spatial temperature patterns that agree with the observation/reanalysis-based patterns shown by WFDEI.

Figure 8 shows the ~~absolute~~ monthly mean precipitation (rainfall and snowfall) differences and pattern correlations for the NE30 and HMA VR simulations and WFDEI. Rainfall is overestimated relative to WFDEI during JJA in southern HMA (up to ~150 mm month^{-1}), particularly in SE-HMA, which is monsoon-dominated and the wettest HMA subregion with summer rainfall sums of 740 mm in WFDEI (Table S2). The interquartile range of the rainfall bias is similar among the CESM grids, whereas the median of the rainfall bias is slightly larger for NE30 than for HMA VR in most subregions. The pattern correlation between WFDEI and CESM are worse~~t~~ during DJF, with correlations of 0.87–0.90, and best during SON, with correlations of 0.93–0.96. The best-performing grid relative to WFDEI varies per season, NE30 is better in DJF and

HMA_VR7 in the other seasons. Snowfall is overestimated in the southern HMA subregions during DJF and MAM (up to ~50 mm month^{-1}), particularly in SW-HMA where winter snowfall sums up to 99 mm in WFDEI (Table S2). The snowfall bias is generally largest for HMA_VR7b, followed by HMA_VR7a and NE30. The snowfall bias is likely related to the cold bias in this region (Figure 7) and to some extent to the changed rain/snow repartitioning temperature thresholds in HMA_VR7b, which favor snowfall. The snowfall (and rainfall) biases could also be a result of the aforementioned uncertainties in WFDEI. Although the ~~absolute~~ snowfall biases are large during DJF and MAM, the pattern correlations suggest that CESM, with correlations of 0.8–0.86, can reasonably simulate the snowfall patterns of WFDEI, with HMA_VR7 performing better than NE30. Only in JJA do the simulated snowfall patterns show a large deviation from the WFDEI snowfall patterns. The NE30 run has the worst performance, with a pattern correlation of 0.37. The HMA_VR7 grid gives pattern correlations of 0.68–0.7, consistent with the improved precipitation shown in Figure 5.

3.4 Snow Depth & Cover

Figure 9 shows the ~~absolute~~ monthly mean snow-cover and snow depth differences and pattern correlations between the NE30 and HMA VR configurations, the observation-based NSIDC dataset, and the ~~re~~analysis-based HARv2~~JRA55~~ dataset. In most HMA subregions, snow cover is overestimated during winter (up to ~40%) and underestimated during summer (up to ~40%). Only in NE-HMA is the NE30 and HMA VR snow cover comparable to the NSIDC snow cover. The HMA VR simulations show some improvements compared to NE30 during spring and summer, but there are no significant differences between HMA_VR7a and HMA_VR7b. The pattern correlations between the NSIDC data and the NE30 and HMA VR runs are worst during JJA, with correlations of 0.69–0.72, and best during DJF, with correlations of 0.88–0.92. In general, HMA_VR7b has the best snow cover followed by HMA_VR7a and NE30. Compared to HARv2 ~~JRA55~~, snow depth is particularly overestimated over SW-HMA during winter and spring (up to ~100~~75~~ mm w.e.), in part because of the cold bias. The snow depth from HMA_VR7a has a smaller bias than NE30, but the snow depth from HMA_VR7b shows a larger bias than HMA_VR7a. The increased bias is likely related to the snow model modifications in HMA_VR7b, including a higher maximum snow depth and changed rain/snow repartitioning thresholds. The pattern correlations show a better performance of NE30 and HMA_VR7 during winter and spring than during summer and autumn. In particular, HMA_VR7b underperforms relative to HARv2~~JRA55~~.

3.5 Surface Energy Balance

Figure 10 shows the annual cycle of surface-energy-balance (SEB) components over glaciated grid cells (encompassing all land units) in HMA. The downwelling, upwelling, and net shortwave radiation (SW_d, SW_u, and SW_{net}, respectively) for NE30 and HMA_VR7 are overestimated relative to CERES-EBAF but generally are closer to JRA55 (Figs. 10a-c, Table 3~~2~~). SW radiation fluxes are higher for HMA_VR7 than for NE30. The downwelling and upwelling longwave radiation (LW_d and LW_u, respectively) for NE30 and HMA_VR7 are generally underestimated relative to CERES-EBAF, particularly in winter (Figs. 10d-e, Table 3~~2~~). In summer, the LW_u simulated by HMA_VR7 agrees more closely with CERES-EBAF than NE30

and JRA55, whereas the LW_d is more accurately simulated by NE30 (relative to CERES-EBAF, Table 3~~2~~). The net LW radiation (LW_{net}) is underestimated relative to CERES-EBAF while NE30 is in a closer agreement with CERES-EBAF than HMA_VR7 (Fig. 10f, Table 3~~2~~). The differences in SW and LW radiation fluxes among the different grids and reference output are likely related to differences in cloud cover. As described in Section 3.2, the cloud cover in CESM is too low, especially over the Tibetan Plateau and in the VR runs. With reduced cloud cover, more solar radiation reaches the surface and less thermal radiation is absorbed, increasing SW_d and reducing LW_d. The reduced cloud cover can also contribute to the cold biases, especially during wintertime when the net radiation is already negative (Table 3). On daily basis, reduced cloud cover could result in more shortwave insolation during the day, and enhanced radiative cooling during the night when the radiative balance is negative. The enhanced radiative cooling could then eventually lead to a (more) negative net daily radiative balance, especially during wintertime when the nights are longer, and the solar inclination angle is lower. Consequently, the surface temperature decreases, contributing to a cold bias.

The seasonal cycle of the sensible and latent heat flux is compared only to JRA55. In summer, the upward sensible heat flux (SHF) is higher for NE30 and HMA_VR7 than for JRA55, whereas the upward latent heat flux (LHF) is lower (Figs. 10g-h, Table 3~~2~~). These biases could be caused by lower snow cover and subsequent lower sublimation and evapotranspiration. Summer surface albedo is lower for NE30 and HMA_VR7 than for JRA55 (Fig. 10i) but is in closer agreement with CERES-EBAF. In winter, the surface albedo for NE30 and HMA_VR7 is overestimated relative to JRA55 and CERES-EBAF, which could be linked to overestimated snow depth (Fig. 9).

The melt heat flux (MHF) (Fig. 10j, Table 3~~2~~) is higher during summer for HMA_VR7 than for NE30 or JRA55. Here, HMA_VR7a has a higher MHF than HMA_VR7b, with more ice melt in summer. The greater cloud cover in HMA_VR7b (relative to HMA_VR7a) reduces SW_d at the surface and increases LW_d, which overall results in lower net radiation (i.e., the sum of SW_{net} and LW_{net}) and reduced melting and heating. NE30 and JRA55 have a lower summer MHF than HMA_VR7 because they are unable to simulate ice melt over High Mountain Asia.

The conductive or ground heat flux (GHF, Figure 10k, Table 3~~2~~) simulated by JRA55 and NE30 is positive in autumn/winter and negative in spring/summer, whereas the GHF simulated by HMA_VR7 is negative only during spring and strongly positive during the other seasons. Here, GHF is positive for heat conduction from the bedrock toward the surface, which usually occurs when the surface is colder than the layers below (van Kampenhout et al., 2020). GHF is typically positive during winter, at night, or after refreezing of snowmelt, and negative during spring/summer and daytime. The combination of a positive winter GHF partly countering the negative radiative balance, and latent and sensible heat fluxes close to zero (Table 3), could trigger a so-called stability-induced cooling feedback (Slater et al., 2001). Via the stability-induced cooling feedback, radiative cooling is enhanced, causing surface temperature to be lower than the overlying air temperature (i.e., a decoupling of the surface from the atmosphere), which could eventually also explain the cold biases. The positive summer GHF simulated by HMA_VR7 is likely not related to refreezing of snowmelt (which is highest in spring and limited during summer, see Fig. 10l, Table 3~~2~~), but rather to extensive ice melt, which requires heat extraction from the environment, and, in turn, also can contribute to cold biases. Greater MHF for HMA_VR7a than for HMA_VR7b

requires a more positive summer GHF. Positive GHF is also observed over the ablation zones of the Greenland ice sheet (GrIS), although this is likely related to high rates of snow refreezing (van Kampenhout et al., 2020).

3.6 Surface Mass Balance

Figure 11 shows the area-averaged glacier surface mass balance derived from geodetical/glaciological observations, WRF-based output, and the HMA VR simulations for three Randolph Glacier Inventory (RGI) regions: Central Asia (NE-HMA + NW-HMA), South Asia West (SW-HMA), and South Asia East (SE-HMA). The observation- and WRF-based SMB are in the same range (between +0.5 – -0.5 m w.e. yr^{-1}), whereas the SMB of HMA_VR7 is too negative. The SMB bias is larger for HMA_VR7a, with SMB values of -2.5 to -4.0 m w.e. yr^{-1}. HMA_VR7b shows significant improvement with SMB values of -0.5 to -2.5 m w.e. yr^{-1}.

SMB improvements over southern and southeastern HMA are also visible in Figure 12, which shows the spatial distribution of mean annual SMB (m w.e. yr^{-1}) for 1979–1998 as simulated by HMA_VR7a and HMA_VR7b. The SMB for HMA_VR7a is mostly negative except for a few small regions in southernmost HMA where a positive SMB is simulated (Figs. 12a, b). The positive SMB in these regions can likely be attributed to high monsoon precipitation. The SMB is mostly negative in southeastern HMA, in part because of inaccuracies in the original glacier-cover dataset. The SMB for HMA_VR7b is less negative for the majority of glaciated grid cells, with the greatest improvements in southeastern HMA (Figs 12c-f), where the updated glacier-cover dataset is based on more accurate glacier outlines and includes glaciers located at altitudes between than 6000 m and 7000 m. Glaciers at these altitudes generally have a more positive SMB than lower-altitude glaciers (Figure 13). Also, HMA_VR7b has more grid cells with a positive SMB, especially in SE-HMA. Compared to HMA_VR7a, the number of grid cells with a positive SMB at the end of a model run nearly triples, from 105 to 299.

Table ~~4~~3 shows the SMB components, which are integrated over the glacier area of the glacier-cover datasets used in the respective HMA VR simulations. To enable comparison between the two simulations, the SMB components of HMA_VR7a have also been integrated over the glacier area of the updated dataset (marked as HMA_VR7a_GC2). The largest positive SMB term in both simulations is precipitation. CESM simulates total annual precipitation of 111 ± 6 Gt yr^{-1} (90 ± 5 Gt yr^{-1}) and 93 ± 4 Gt yr^{-1} in HMA_VR7a (HMA_VR7a_GC2) and HMA_VR7b, respectively. Integrated over the updated dataset, total annual precipitation is higher in HMA_VR7b, likely because of increased snowfall and rainfall during spring in southern HMA (Figure 8). For instance, in SE-HMA, rainfall and snowfall increase from 131 mm $month^{-1}$ in HMA_VR7a to 148 mm $month^{-1}$ in HMA_VR7b, possibly because of the tunings on cloud cover and the application of a newer microphysics scheme. The second largest positive SMB term is refreezing, which increases from 29 ± 2 Gt yr^{-1} in HMA_V7a_GC2 to 32 ± 2 Gt yr^{-1} in HMA_VR7b. The increase in refreezing can mainly be attributed to the greater maximum snow depth.

The largest SMB loss term in the HMA VR simulations is total melt, which is dominated by ice melt. The total (ice) melt volumes decrease from 432 ± 23 Gt yr^{-1} (356 ± 26 Gt yr^{-1}) for HMA_VR7a_GC2 to 324 ± 18 Gt yr^{-1} (228 ± 20 Gt yr^{-1})

for HMA_VR7b. The decreased melt can be attributed to several factors, including 1) a decrease in net radiation with increased cloud cover, 2) increased snowfall and higher maximum allowed snow depth, which increase refreezing capacity and snow persistence, 3) improved accuracy of glacier-elevation distribution with the updated glacier-cover dataset, and 4) a higher albedo for bare ice. The latter increases the upwelling shortwave radiation. From Figure 10 and Table 3~~2~~, it is, however, not apparent that upwelling shortwave radiation increases between the two simulations, because SEB components in Figure 10 and Table 3~~2~~ are representative for the mean of all land units in glaciated grid cells. However, when selecting grid cells with a higher ice fraction (i.e., higher than 25%), the upwelling shortwave radiation increases from 104 W m^{-2} for HMA_VR7a to 113 W m^{-2} for HMA_VR7b, as a result of a higher bare-ice albedo. The second largest negative SMB term, sublimation and/or evaporation, is 12 Gt yr^{-1} for both simulations. Overall, mass loss exceeds accumulation, giving a negative SMB. The integrated SMB is -352 ± 27 Gt yr^{-1} for HMA_VR7a_GC2 and -224 ± 21 Gt yr^{-1} for HMA_VR7b. The latter value is about 1.2 times higher than the Greenland ice sheet SMB (-182 ± 45 Gt yr^{-1}) and 7 times higher than the Antarctic ice sheet SMB (-32 ± 4 Gt yr^{-1}) for 2003–2016 (Lenaerts et al., 2019) (The HMA ranges here represent one standard deviation, whereas Lenaerts et al. (2019) stated ranges with two standard deviations). Both values simulated on the HMA_VR7 grid are much more negative than the observed ranges of -13 ± 17 Gt yr^{-1} and -19 ± 2.5 Gt yr^{-1} for 1979–1998 and 2000–2015/2016, respectively (Brun et al., 2017; Shean et al., 2020; Zemp et al., 2019).

3.7 Future Directions

Although many cryospheric-hydrological variables improve with increasing resolution, and VR-CESM can simulate positive SMB in parts of HMA, the negative SMB bias is cause for concern and suggests that model improvements are needed. There are several possible explanations for this bias. One explanation is the warm temperature bias over Central Asia, particularly over the Tibetan Plateau as suggested in Sections 3.1, 3.2, and 3.3. This warm bias could be related to underestimated cloud cover, which results in a higher net surface radiation due to increased downwelling solar radiation (partly offset by decreased downwelling longwave radiation, as suggested in Section 3.5). Improved convection and cloud parameterization schemes are needed. To make progress on the parameterization problem, we plan to carry out additional experiments nudging the upper vertical levels of CAM for variables such as horizontal wind, temperature, and humidity from ERA-Interim or ERA5, as previously done with WRF in HMA (de Kok et al., 2020). CAM contains flexible nudging capabilities (Wu et al., 2022; Kruse et al., 2022), with options for nudging over a particular region or level. The nudging tendencies by definition are collocated with the model bias, and an analysis of those tendencies constrains how the physics should interact with the dynamics at a particular grid resolution in order to provide a more realistic large-scale state, e.g., avoiding the anomalous large-scale subsidence in the free-running VR runs responsible for cloud biases on the north side of the Tibetan Plateau. The nudging experiments also provide us with an opportunity to analyze the simulated surface mass balance given a realistic atmospheric state, thereby helping to further isolate the cause of the deficiencies to the atmosphere or surface components.

Another reason for the negative SMB bias could be a lack of representation of surface processes in CLM that are important in complex mountain environments. For example, CLM neglects the role of aspect and orientation in the SEB (via solar illumination), and the glacier SMB. Wang et al. (2022) found out that 27.19% of the HMA glaciers are subject to topographic shading, particularly for the north-facing glaciers of the Tibetan Plateau and the surrounding mountain ranges to the northwest and northeast (i.e., Kunlun Shan, Qilian Shan). Hillslope parameterization schemes (e.g., Swenson et al., 2019), which include the effects of aspect and orientation of a hillslope on the incoming solar radiation, could improve the simulation of SEB and SMB. Further, CLM does not represent debris cover on mountain glaciers. About 12%–13% of the glaciers in HMA are at least partly covered by supraglacial debris which, depending on its thickness, can accelerate or reduce glacial melt (by reducing surface albedo or insulating the surface, respectively) (e.g., Herreid and Pellicciotti, 2020). Including debris cover in CLM surface datasets and adding debris-related glacial melt processes could be beneficial. Another weak point is the simulation of orographic precipitation in CLM. Currently, precipitation can be repartitioned as snow or rain based on downscaled air temperature, but the effect of topography on total precipitation is ignored and the repartitioning applies fixed rain-snow temperature thresholds. Topography-based subgrid parameterizations such as the Elevation Ratio Weighted Method (ERWM; Tesfa et al., 2020) and more advanced rain-snow repartitioning schemes applying temperature-humidity-surface pressure-based rain-snow thresholds (Jennings et al., 2018) could improve the model's skill in simulating high-altitude precipitation.

The negative SMB bias could also be related to the elevation-class (EC) downscaling scheme in CLM and the way CLM and CAM are coupled. Figure 1~~4~~5 shows the relation between grid-cell-mean SMB and glacier fraction (GCF) in 15 elevation zones at intervals of 250 m (based on the grid-cell-mean elevation). At lower elevations where glacier tongues reside, the glacier fraction is relatively low, whereas the most highly glaciated grid cells (with GCF higher than 90%) have a mean grid cell elevation above 5000 m. In most elevation zones, SMB declines with decreasing glacier fraction. In some zones, such as 4000 m – 4250 m, the SMB is more than 2 m w.e. yr^{-1} lower for sparsely glaciated cells (GCF of 0–10%) than for highly glaciated cells (GCF of 90–100%). In sparsely glaciated cells, elevation downscaling is only applied over glacier land units, whereas vegetated land units are excluded from downscaling. Moreover, the coupling between CLM and CAM is based on the homogenized state of a CLM grid cell, i.e., the average over all land units within the grid cell. This means that in grid cells with small ice fractions, the impact of glaciers is limited, and the mean depends mainly on fluxes from vegetated land units. CAM receives this homogenized state and subsequently couples back to CLM, with downscaling of a few atmospheric variables, such as near-surface temperature. If the glacier patch lies higher than the grid-cell-mean elevation (and thus the elevation of the vegetated land unit), the glacier land unit sees a cooler air temperature than the vegetated land unit. However, the atmospheric temperature coupled to CLM could be dominated by the lower-lying and warmer vegetated land unit. This could result in warmer glacier temperatures that make the SMB more negative. One potential solution is to apply elevation downscaling over all land units using the hillslope model of Swenson et al. (2019). Another is to improve the subgrid coupling between CLM and CAM by introducing CLM patch information into CAM; this is the focus of the CLASP (Coupling of Land and Atmosphere Subgrid Parameterizations) project (Waterman et al., 2022). The necessity to improve

land-atmosphere coupling (via elevation downscaling) is also suggested by offline 3-year (1979–1981) CLM simulations performed on the HMA_VR7 grid and driven by observation/reanalysis-based meteorological forcings of the Global Soil Wetness Project version 3 (GSWP3; Dirmeyer et al., 2006), a default offline mode in CLM. The offline CLM simulations (referred as HMALOa and HMALOb i.e., following the HMA_VR7a and HMA_VR7b settings, respectively) show likewise a declining SMB with decreasing glacier fraction (Figure S3), which suggests that improvement of land-atmosphere coupling is crucial. The offline CLM simulations show nonetheless that the colder and wetter surface climate in the HMA_VR simulations help to reduce the SMB bias (Figures S4 and S5, Table S3).

4. Conclusions

We have investigated the ability of the variable-resolution Community Earth System Model to simulate cryospheric-hydrological variables such as glacier surface mass balance and snow conditions over High Mountain Asia. To this end, we developed a new VR grid with regional refinement up to 7 km over HMA. With this grid, we ran two 20-year (1979–1998) model simulations. The second model simulation includes an updated glacier-cover dataset and several atmosphere and land model modifications. We evaluated the results by comparison to gridded outputs derived from a globally uniform 1° CESM grid, reanalysis-, satellite-, and observation-based datasets, and an WRF-based glacier model.

The evaluations show that the large-scale circulation on the HMA_VR7 grid generally compares well to ERA5, but with an upper-troposphere warm temperature bias at mid-latitudes during summer. This warm bias grows with increasing horizontal resolution (+2 K for NE30 and +3 K for HMA_VR7). Further, the HMA VR runs have less cloud cover than NE30 runs, which is likely related to enhanced subsidence driven by more intense monsoonal circulation, and to the shorter physics time step in the HMA runs. The HMA VR runs also have a summertime warm temperature bias (up to about +2.5 °C) at the surface, but this bias is smaller than for NE30, likely because of elevation downscaling. Most~~Western~~ HMA subregions have cold temperature biases during winter and to lesser extent during other seasons; these biases grow with increasing resolution. Overall, the HMA VR runs simulate rainfall, snowfall, snow cover, and snow depth better than NE30, but with some biases. Rainfall biases occur mainly in monsoon-dominated regions, whereas snowfall, snow cover, and snow depth biases are largest during winter and spring in southwestern HMA, in part because of the cold temperature bias and the HMA_VR7b model modifications. Snow cover is underestimated during summer but agrees better than NE30 with NSIDC snow cover.

The HMA VR runs have more downwelling shortwave radiation and less downwelling longwave radiation compared to NE30, JRA55 and CERES-EBAF. This can be attributed to negative cloud-cover biases that reduce longwave absorption and lower the albedo. The HMA VR runs have greater net radiation at the surface, resulting in higher melting and a positive (upward) conductive heat flux. The high volumes of snow and ice melting translate into an SMB that is more negative than observation-based glaciological/geodetical mass balances and WRF-based results. The HMA_VR7b simulation has a smaller

SMB bias than HMA_VR7a, with an integrated SMB over glaciers of -224 ± 21 Gt yr^{-1}, compared to -352 ± 28 Gt yr^{-1} for HMA_VR7a.

This study shows that VR-CESM generally reduces climatological biases relative to a coarse-resolution CESM grid and could be a useful tool for simulating cryospheric-hydrological variables, such as glacier SMB, in HMA. However, improvements are still needed to reduce cloud-cover and temperature biases, improve the model physics and land-atmosphere coupling, and thereby simulate SMB more accurately. This study could be a starting point for simulating cryospheric-hydrological variables in HMA and other mountain glacier regions with VR-CESM and other GCMs and ESMs.

Code and Data Availability.

Publicly available data are stored in two separate data archives on Zenodo. The first archive (https://doi.org/10.5281/zenodo.7864689) contains the model scripts and files that were used to create the updated glacier cover dataset. The second archive (https://doi.org/10.5281/zenodo.7864633) contains the NE30 and HMA VR7 grid variables that were used to generate most of the figures in this manuscript. The remainder of the data are available on request.~~Data will be available before publication in Zenodo.~~

Author Contributions.

R.R. Wijngaard, A. R. Herrington, W.H. Lipscomb, and G. R. Leguy designed the study. R.R. Wijngaard and A.R. Herrington modified the model code as needed. R.R. Wijngaard ran the model. R.R. Wijngaard and A.R. Herrington analyzed model results and prepared the text and figures. All authors contributed to the final text.

Competing Interests.

The authors declare that they have no conflict of interest.

Acknowledgements.

We would like to thank the reviewers for their constructive remarks and suggestions that helped us to improve the paper significantly. We greatly acknowledge Samar Minallah, Leo van Kampenhout, and Bill Sacks for the helpful discussions and support. This work is supported by the National Research Foundation of Korea (NRF) grant funded by the Korea government (MSIT) (NRF-2018R1A5A1024958). A. R. Herrington, W. H. Lipscomb, and G. R. Leguy are supported by the National Center for Atmospheric Research, which is a major facility sponsored by the National Science Foundation under cooperative agreement no. 1852977. Computing and data storage resources, including the Cheyenne supercomputer (https://doi.org/10.5065/D6RX99HX, Computational and Information Systems Laboratory, 2019), were provided by the Computational and Information Systems Laboratory (CISL) at NCAR.

References

Bambach, N. E., Rhoades, A. M., Hatchett, B. J., Jones, A. D., Ullrich, P. A., and Zarzycki, C. M.: Projecting climate change in South America using variable-resolution Community Earth System Model: An application to Chile, International Journal of Climatology, https://doi.org/10.1002/joc.7379, 2021.

Beljaars, A. C. M., Brown, A. R., and Wood, N.: A new parametrization of turbulent orographic form drag, Quarterly Journal of the Royal Meteorological Society, 130, https://doi.org/10.1256/qj.03.73, 2004.

Bogenschutz, P. A., Gettelman, A., Morrison, H., Larson, V. E., Craig, C., and Schanen, D. P.: Higher-order turbulence closure and its impact on climate simulations in the community atmosphere model, J Clim, 26, https://doi.org/10.1175/JCLI-D-13-00075.1, 2013.

Bonekamp, P. N. J., de Kok, R. J., Collier, E., and Immerzeel, W. W.: Contrasting Meteorological Drivers of the Glacier Mass Balance Between the Karakoram and Central Himalaya, Front Earth Sci (Lausanne), 7, https://doi.org/10.3389/feart.2019.00107, 2019.

Brodzik, M. J. and Armstrong, R.: Northern Hemisphere EASE-Grid 2.0 Weekly Snow Cover and Sea Ice Extent. Version 4., Boulder, Colorado USA: NASA DAAC at the National Snow and Ice Data Center., https://doi.org/https://doi.org/10.5067/P7O0HGJLYUQU, 2013.

Brun, F., Berthier, E., Wagnon, P., Kääb, A., and Treichler, D.: A spatially resolved estimate of High Mountain Asia glacier mass balances from 2000 to 2016, Nat Geosci, 10, 668–673, https://doi.org/10.1038/ngeo2999, 2017.

Cannon, F., Carvalho, L. M. V., Jones, C., and Bookhagen, B.: Multi-annual variations in winter westerly disturbance activity affecting the Himalaya, Clim Dyn, 44, 441–455, https://doi.org/10.1007/s00382-014-2248-8, 2015.

Collier, E., Mölg, T., Maussion, F., Scherer, D., Mayer, C., and Bush, A. B. G.: High-resolution interactive modelling of the mountain glacier–atmosphere interface: an application over the Karakoram, Cryosphere, 7, 779–795, https://doi.org/10.5194/tc-7-779-2013, 2013.

Danabasoglu, G., Lamarque, J. F., Bacmeister, J., Bailey, D. A., DuVivier, A. K., Edwards, J., Emmons, L. K., Fasullo, J., Garcia, R., Gettelman, A., Hannay, C., Holland, M. M., Large, W. G., Lauritzen, P. H., Lawrence, D. M., Lenaerts, J. T. M., Lindsay, K., Lipscomb, W. H., Mills, M. J., Neale, R., Oleson, K. W., Otto-Bliesner, B., Phillips, A. S., Sacks, W., Tilmes, S., van Kampenhout, L., Vertenstein, M., Bertini, A., Dennis, J., Deser, C., Fischer, C., Fox-Kemper, B., Kay, J. E., Kinnison, D., Kushner, P. J., Larson, V. E., Long, M. C., Mickelson, S., Moore, J. K., Nienhouse, E., Polvani, L., Rasch, P. J., and Strand, W. G.: The Community Earth System Model Version 2 (CESM2), J Adv Model Earth Syst, 12, https://doi.org/10.1029/2019MS001916, 2020.

Danielson, J. J. and Gesch, D. B.: Global Multi-resolution Terrain Elevation Data 2010 (GMTED2010), U.S. Geological Survey Open-File Report 2011-1073, 2011.

Dirmeyer, P. A., Gao, X., Zhao, M., Guo, Z., Oki, T., and Hanasaki, N.: GSWP-2: Multimodel analysis and implications for our perception of the land surface, Bull Am Meteorol Soc, 87, https://doi.org/10.1175/BAMS-87-10-1381, 2006.

Flanner, M. G. and Zender, C. S.: Snowpack radiative heating: Influence on Tibetan Plateau climate, Geophys Res Lett, 32, L06501, https://doi.org/10.1029/2004GL022076, 2005.

Flanner, M. G., Zender, C. S., Randerson, J. T., and Rasch, P. J.: Present-day climate forcing and response from black carbon in snow, Journal of Geophysical Research Atmospheres, 112, https://doi.org/10.1029/2006JD008003, 2007.

Frey, H., Haeberli, W., Linsbauer, A., Huggel, C., and Paul, F.: A multi-level strategy for anticipating future glacier lake formation and associated hazard potentials, Natural Hazards and Earth System Sciences, 10, 339–352, https://doi.org/10.5194/nhess-10-339-2010, 2010.

Gates, W. L., Boyle, J. S., Covey, C., Dease, C. G., Doutriaux, C. M., Drach, R. S., Fiorino, M., Gleckler, P. J., Hnilo, J. J., Marlais, S. M., Phillips, T. J., Potter, G. L., Santer, B. D., Sperber, K. R., Taylor, K. E., and Williams, D. N.: An Overview of the Results of the Atmospheric Model Intercomparison Project (AMIP I), Bull Am Meteorol Soc, 80, 29–55, https://doi.org/10.1175/1520-0477(1999)080<0029:AOOTRO>2.0.CO;2, 1999.

Gettelman, A. and Morrison, H.: Advanced two-moment bulk microphysics for global models. Part I: Off-line tests and comparison with other schemes, J Clim, 28, https://doi.org/10.1175/JCLI-D-14-00102.1, 2015.

Gettelman, A., Callaghan, P., Larson, V. E., Zarzycki, C. M., Bacmeister, J. T., Lauritzen, P. H., Bogenschutz, P. A., and Neale, R. B.: Regional Climate Simulations With the Community Earth System Model, J Adv Model Earth Syst, 10, 1245–1265, https://doi.org/10.1002/2017MS001227, 2018.

Gettelman, A., Hannay, C., Bacmeister, J. T., Neale, R. B., Pendergrass, A. G., Danabasoglu, G., Lamarque, J. F., Fasullo, J. T., Bailey, D. A., Lawrence, D. M., and Mills, M. J.: High Climate Sensitivity in the Community Earth System Model Version 2 (CESM2), Geophys Res Lett, 46, https://doi.org/10.1029/2019GL083978, 2019a.

Gettelman, A., Morrison, H., Thayer-Calder, K., and Zarzycki, C. M.: The Impact of Rimed Ice Hydrometeors on Global and Regional Climate, J Adv Model Earth Syst, 11, https://doi.org/10.1029/2018MS001488, 2019b.

Goldewijk, K. K., Beusen, A., Doelman, J., and Stehfest, E.: Anthropogenic land use estimates for the Holocene - HYDE 3.2, Earth Syst Sci Data, 9, https://doi.org/10.5194/essd-9-927-2017, 2017.

Gu, H., Wang, G., Yu, Z., and Mei, R.: Assessing future climate changes and extreme indicators in east and south Asia using the RegCM4 regional climate model, Clim Change, 114, https://doi.org/10.1007/s10584-012-0411-y, 2012.

Guba, O., Taylor, M. A., Ullrich, P. A., Overfelt, J. R., and Levy, M. N.: The spectral element method (SEM) on variable-resolution grids: evaluating grid sensitivity and resolution-aware numerical viscosity, Geosci Model Dev, 7, 2803–2816, https://doi.org/10.5194/gmd-7-2803-2014, 2014.

Herreid, S. and Pellicciotti, F.: The state of rock debris covering Earth's glaciers, Nat Geosci, 13, https://doi.org/10.1038/s41561-020-0615-0, 2020.

Herrington, A. R. and Reed, K. A.: On resolution sensitivity in the Community Atmosphere Model, Quarterly Journal of the Royal Meteorological Society, 146, 3789–3807, https://doi.org/10.1002/qj.3873, 2020.

Herrington, A. R., Lauritzen, P. H., Lofverstrom, M., Lipscomb, W. H., Gettelman, A., and Taylor, M. A.: Impact of grids and dynamical cores in CESM2.2 on the surface mass balance of the Greenland Ice Sheet, J Adv Model Earth Syst, https://doi.org/10.1029/2022MS003192, 2022.

Hersbach, H., Bell, B., Berrisford, P., Hirahara, S., Horányi, A., Muñoz-Sabater, J., Nicolas, J., Peubey, C., Radu, R., Schepers, D., Simmons, A., Soci, C., Abdalla, S., Abellan, X., Balsamo, G., Bechtold, P., Biavati, G., Bidlot, J., Bonavita, M., De Chiara, G., Dahlgren, P., Dee, D., Diamantakis, M., Dragani, R., Flemming, J., Forbes, R., Fuentes, M., Geer, A., Haimberger, L., Healy, S., Hogan, R. J., Hólm, E., Janisková, M., Keeley, S., Laloyaux, P., Lopez, P., Lupu, C., Radnoti, G., de Rosnay, P., Rozum, I., Vamborg, F., Villaume, S., and Thépaut, J. N.: The ERA5 global reanalysis, Quarterly Journal of the Royal Meteorological Society, 146, https://doi.org/10.1002/qj.3803, 2020.

Hock, R., Rasul, G., Adler, C., Cáceres, B., Gruber, S., Hirabayashi, Y., Jackson, M., Kääb, A., Kang, S., Kutuzov, S., Milner, A., Molau, U., Morin, S., Orlove, B., and Steltzer, H. I.: High Mountain Areas, in: IPCC Special Report on the Ocean and Cryosphere in a Changing Climate, edited by: Pörtner, H.-O., Roberts, D. C., Masson-Delmotte, V., Zhai, P., Tignor, M., Poloczanska, E., Mintenbeck, K., Alegría, A., Nicolai, M., Okem, A., Petzold, J., Rama, B., and Weyer, N. M., IPCC Intergovernmental Panel on Climate Change, Geneva, Switzerland, 2019.

Huang, X., Rhoades, A. M., Ullrich, P. A., and Zarzycki, C. M.: An evaluation of the variable-resolution CESM for modeling California's climate, J Adv Model Earth Syst, 8, 345–369, https://doi.org/10.1002/2015MS000559, 2016.

Hurrell, J. W., Hack, J. J., Shea, D., Caron, J. M., and Rosinski, J.: A new sea surface temperature and sea ice boundary dataset for the community atmosphere model, J Clim, 21, https://doi.org/10.1175/2008JCLI2292.1, 2008.

Hurtt, G. C., Chini, L., Sahajpal, R., Frolking, S., Bodirsky, B. L., Calvin, K., Doelman, J. C., Fisk, J., Fujimori, S., Goldewijk, K. K., Hasegawa, T., Havlik, P., Heinimann, A., Humpenöder, F., Jungclaus, J., Kaplan, J. O., Kennedy, J., Krisztin, T., Lawrence, D., Lawrence, P., Ma, L., Mertz, O., Pongratz, J., Popp, A., Poulter, B., Riahi, K., Shevliakova, E., Stehfest, E., Thornton, P., Tubiello, F. N., van Vuuren, D. P., and Zhang, X.: Harmonization of global land use change and management for the period 850-2100 (LUH2) for CMIP6, Geosci Model Dev, 13, https://doi.org/10.5194/gmd-13-5425-2020, 2020.

Immerzeel, W. W., Wanders, N., Lutz, A. F., Shea, J. M., and Bierkens, M. F. P.: Reconciling high altitude precipitation with glacier mass balances and runoff, Hydrol Earth Syst Sci, 12, 4755–4784, https://doi.org/10.5194/hessd-12-4755-2015, 2015.

Immerzeel, W. W., Lutz, A. F., Andrade, M., Bahl, A., Biemans, H., Bolch, T., Hyde, S., Brumby, S., Davies, B. J., Elmore, A. C., Emmer, A., Feng, M., Fernández, A., Haritashya, U., Kargel, J. S., Koppes, M., Kraaijenbrink, P. D. A., Kulkarni, A. v., Mayewski, P. A., Nepal, S., Pacheco, P., Painter, T. H., Pellicciotti, F., Rajaram, H., Rupper, S., Sinisalo, A., Shrestha, A. B., Viviroli, D., Wada, Y., Xiao, C., Yao, T., and Baillie, J. E. M.: Importance and vulnerability of the world's water towers, Nature, https://doi.org/10.1038/s41586-019-1822-y, 2020.

Jeevanjee, N.: Vertical Velocity in the Gray Zone, J Adv Model Earth Syst, 9, https://doi.org/10.1002/2017MS001059, 2017.

Jennings, K. S., Winchell, T. S., Livneh, B., and Molotch, N. P.: Spatial variation of the rain-snow temperature threshold across the Northern Hemisphere, Nat Commun, 9, https://doi.org/10.1038/s41467-018-03629-7, 2018.

van Kampenhout, L., Lenaerts, J. T. M., Lipscomb, W. H., Sacks, W. J., Lawrence, D. M., Slater, A. G., and van den Broeke, M. R.: Improving the Representation of Polar Snow and Firn in the Community Earth System Model, J Adv Model Earth Syst, 9, 2583–2600, https://doi.org/10.1002/2017MS000988, 2017.

van Kampenhout, L., Rhoades, A. M., Herrington, A. R., Zarzycki, C. M., Lenaerts, J. T. M., Sacks, W. J., and van den Broeke, M. R.: Regional grid refinement in an Earth system model: impacts on the simulated Greenland surface mass balance, Cryosphere, 13, 1547–1564, https://doi.org/10.5194/tc-13-1547-2019, 2019.

van Kampenhout, L., Lenaerts, J. T. M., Lipscomb, W. H., Lhermitte, S., Noël, B., Vizcaíno, M., Sacks, W. J., and van den Broeke, M. R.: Present-Day Greenland Ice Sheet Climate and Surface Mass Balance in CESM2, J Geophys Res Earth Surf, 125, https://doi.org/10.1029/2019JF005318, 2020.

Kato, S., Rose, F. G., Rutan, D. A., Thorsen, T. J., Loeb, N. G., Doelling, D. R., Huang, X., Smith, W. L., Su, W., and Ham, S. H.: Surface irradiances of edition 4.0 Clouds and the Earth's Radiant Energy System (CERES) Energy Balanced and Filled (EBAF) data product, J Clim, 31, https://doi.org/10.1175/JCLI-D-17-0523.1, 2018.

Kobayashi, S., Ota, Y., Harada, Y., Ebita, A., Moriya, M., Onoda, H., Onogi, K., Kamahori, H., Kobayashi, C., Endo, H., Miyaoka, K., and Kiyotoshi, T.: The JRA-55 reanalysis: General specifications and basic characteristics, Journal of the Meteorological Society of Japan, 93, https://doi.org/10.2151/jmsj.2015-001, 2015.

de Kok, R. J., Kraaijenbrink, P. D. A., Tuinenburg, O. A., Bonekamp, P. N. J., and Immerzeel, W. W.: Towards understanding the pattern of glacier mass balances in High Mountain Asia using regional climatic modelling, Cryosphere, 14, 3215–3234, https://doi.org/10.5194/tc-14-3215-2020, 2020.

Körner, C., Jetz, W., Paulsen, J., Payne, D., Rudmann-Maurer, K., and M. Spehn, E.: A global inventory of mountains for bio-geographical applications, Alp Bot, 127, https://doi.org/10.1007/s00035-016-0182-6, 2017.

Kraaijenbrink, P. D. A., Bierkens, M. F. P., Lutz, A. F., and Immerzeel, W. W.: Impact of a global temperature rise of 1.5 degrees Celsius on Asia's glaciers, Nature, 549, 257–260, https://doi.org/10.1038/nature23878, 2017.

Kruse, C. G., Bacmeister, J. T., Zarzycki, C. M., Larson, V. E., and Thayer-Calder, K.: Do Nudging Tendencies Depend on the Nudging Timescale Chosen in Atmospheric Models?, J Adv Model Earth Syst, 14, https://doi.org/10.1029/2022MS003024, 2022.

Lalande, M., Ménégoz, M., Krinner, G., Naegeli, K., and Wunderle, S.: Climate change in the High Mountain Asia in CMIP6, Earth System Dynamics, 12, https://doi.org/10.5194/esd-12-1061-2021, 2021.

Lauritzen, P. H., Bacmeister, J. T., Callaghan, P. F., and Taylor, M. A.: NCAR_Topo (v1.0): NCAR global model topography generation software for unstructured grids, Geosci Model Dev, 8, 3975–3986, https://doi.org/10.5194/gmd-8-3975-2015, 2015.

Lauritzen, P. H., Nair, R. D., Herrington, A. R., Callaghan, P., Goldhaber, S., Dennis, J. M., Bacmeister, J. T., Eaton, B. E., Zarzycki, C. M., Taylor, M. A., Ullrich, P. A., Dubos, T., Gettelman, A., Neale, R. B., Dobbins, B., Reed, K. A., Hannay, C.,

Medeiros, B., Benedict, J. J., and Tribbia, J. J.: NCAR Release of CAM-SE in CESM2.0: A Reformulation of the Spectral Element Dynamical Core in Dry-Mass Vertical Coordinates With Comprehensive Treatment of Condensates and Energy, J Adv Model Earth Syst, 10, https://doi.org/10.1029/2017MS001257, 2018.

Lawrence, D. M., Fisher, R. A., Koven, C. D., Oleson, K. W., Swenson, S. C., Bonan, G., Collier, N., Ghimire, B., Kampenhout, L., Kennedy, D., Kluzek, E., Lawrence, P. J., Li, F., Li, H., Lombardozzi, D., Riley, W. J., Sacks, W. J., Shi, M., Vertenstein, M., Wieder, W. R., Xu, C., Ali, A. A., Badger, A. M., Bisht, G., Broeke, M., Brunke, M. A., Burns, S. P., Buzan, J., Clark, M., Craig, A., Dahlin, K., Drewniak, B., Fisher, J. B., Flanner, M., Fox, A. M., Gentine, P., Hoffman, F., Keppel-Aleks, G., Knox, R., Kumar, S., Lenaerts, J., Leung, L. R., Lipscomb, W. H., Lu, Y., Pandey, A., Pelletier, J. D., Perket, J., Randerson, J. T., Ricciuto, D. M., Sanderson, B. M., Slater, A., Subin, Z. M., Tang, J., Thomas, R. Q., Val Martin, M., and Zeng, X.: The Community Land Model Version 5: Description of New Features, Benchmarking, and Impact of Forcing Uncertainty, J Adv Model Earth Syst, 11, 4245–4287, https://doi.org/10.1029/2018MS001583, 2019.

Lenaerts, J. T. M., Vizcaino, M., Fyke, J., van Kampenhout, L., and van den Broeke, M. R.: Present-day and future Antarctic ice sheet climate and surface mass balance in the Community Earth System Model, Clim Dyn, 47, 1367–1381, https://doi.org/10.1007/s00382-015-2907-4, 2016.

Lenaerts, J. T. M., Medley, B., van den Broeke, M. R., and Wouters, B.: Observing and Modeling Ice Sheet Surface Mass Balance, Reviews of Geophysics, 57, https://doi.org/10.1029/2018RG000622, 2019.

Li, D., Lu, X., Walling, D. E., Zhang, T., Steiner, J. F., Wasson, R. J., Harrison, S., Nepal, S., Nie, Y., Immerzeel, W. W., Shugar, D. H., Koppes, M., Lane, S., Zeng, Z., Sun, X., Yegorov, A., and Bolch, T.: High Mountain Asia hydropower systems threatened by climate-driven landscape instability, Nat Geosci, 15, 520–530, https://doi.org/10.1038/s41561-022-00953-y, 2022.

Lipscomb, W. H., Fyke, J. G., Vizcaíno, M., Sacks, W. J., Wolfe, J., Vertenstein, M., Craig, A., Kluzek, E., and Lawrence, D. M.: Implementation and Initial Evaluation of the Glimmer Community Ice Sheet Model in the Community Earth System Model, J Clim, 26, 7352–7371, https://doi.org/10.1175/JCLI-D-12-00557.1, 2013.

Lipscomb, W. H., Price, S. F., Hoffman, M. J., Leguy, G. R., Bennett, A. R., Bradley, S. L., Evans, K. J., Fyke, J. G., Kennedy, J. H., Perego, M., Ranken, D. M., Sacks, W. J., Salinger, A. G., Vargo, L. J., and Worley, P. H.: Description and evaluation of the Community Ice Sheet Model (CISM) v2.1, Geosci Model Dev, 12, https://doi.org/10.5194/gmd-12-387-2019, 2019.

Liu, W., Ullrich, P. A., Guba, O., Caldwell, P. M., and Keen, N. D.: An Assessment of Nonhydrostatic and Hydrostatic Dynamical Cores at Seasonal Time Scales in the Energy Exascale Earth System Model (E3SM), J Adv Model Earth Syst, 14, https://doi.org/10.1029/2021MS002805, 2022.

Liu, X., Ma, P. L., Wang, H., Tilmes, S., Singh, B., Easter, R. C., Ghan, S. J., and Rasch, P. J.: Description and evaluation of a new four-mode version of the Modal Aerosol Module (MAM4) within version 5.3 of the Community Atmosphere Model, Geosci Model Dev, 9, https://doi.org/10.5194/gmd-9-505-2016, 2016.

Loeb, N. G., Doelling, D. R., Wang, H., Su, W., Nguyen, C., Corbett, J. G., Liang, L., Mitrescu, C., Rose, F. G., and Kato, S.: Clouds and the Earth'S Radiant Energy System (CERES) Energy Balanced and Filled (EBAF) top-of-atmosphere (TOA) edition-4.0 data product, J Clim, 31, https://doi.org/10.1175/JCLI-D-17-0208.1, 2018.

Lutz, A. F., ter Maat, H. W., Wijngaard, R. R., Biemans, H., Syed, A., Shrestha, A. B., Wester, P., and Immerzeel, W. W.: South Asian river basins in a 1.5 °C warmer world, Reg Environ Change, 19, https://doi.org/10.1007/s10113-018-1433-4, 2019.

Lutz, A. F., Immerzeel, W. W., Siderius, C., Wijngaard, R. R., Nepal, S., Shrestha, A. B., Wester, P., and Biemans, H.: South Asian agriculture increasingly dependent on meltwater and groundwater, Nat Clim Chang, 12, 566–573, https://doi.org/10.1038/s41558-022-01355-z, 2022.

Marzeion, B., Hock, R., Anderson, B., Bliss, A., Champollion, N., Fujita, K., Huss, M., Immerzeel, W. W., Kraaijenbrink, P., Malles, J., Maussion, F., Radić, V., Rounce, D. R., Sakai, A., Shannon, S., Wal, R., and Zekollari, H.: Partitioning the Uncertainty of Ensemble Projections of Global Glacier Mass Change, Earths Future, 8, https://doi.org/10.1029/2019EF001470, 2020.

Mölg, T. and Kaser, G.: A new approach to resolving climate-cryosphere relations: Downscaling climate dynamics to glacier-scale mass and energy balance without statistical scale linking, J Geophys Res, 116, D16101, https://doi.org/10.1029/2011JD015669, 2011.

Muntjewerf, L., Sacks, W. J., Lofverstrom, M., Fyke, J., Lipscomb, W. H., Ernani da Silva, C., Vizcaino, M., Thayer-Calder, K., Lenaerts, J. T. M., and Sellevold, R.: Description and Demonstration of the Coupled Community Earth System Model v2 – Community Ice Sheet Model v2 (CESM2-CISM2), J Adv Model Earth Syst, 13, https://doi.org/10.1029/2020MS002356, 2021.

Nie, Y., Pritchard, H. D., Liu, Q., Hennig, T., Wang, W., Wang, X., Liu, S., Nepal, S., Samyn, D., Hewitt, K., and Chen, X.: Glacial change and hydrological implications in the Himalaya and Karakoram, Nat Rev Earth Environ, 2, 91–106, https://doi.org/10.1038/s43017-020-00124-w, 2021.

Oleson, K. W., Lawrence, D. M., and Bonan, G. B.: Technical description of version 4.5 of the Community Land Model (CLM). Ncar Tech. Note NCAR/TN-503+STR. National Center for Atmospheric Research, Boulder, Geophys Res Lett, 37, 2013.

Orsolini, Y., Wegmann, M., Dutra, E., Liu, B., Balsamo, G., Yang, K., de Rosnay, P., Zhu, C., Wang, W., Senan, R., and Arduini, G.: Evaluation of snow depth and snow cover over the Tibetan Plateau in global reanalyses using in situ and satellite remote sensing observations, Cryosphere, 13, 2221–2239, https://doi.org/10.5194/tc-13-2221-2019, 2019.

Palazzi, E., Von Hardenberg, J., Terzago, S., and Provenzale, A.: Precipitation in the Karakoram-Himalaya: a CMIP5 view, Clim Dyn, 45, 21–45, https://doi.org/10.1007/s00382-014-2341-z, 2015.

Rahimi, S. R., Wu, C., Liu, X., and Brown, H.: Exploring a Variable-Resolution Approach for Simulating Regional Climate Over the Tibetan Plateau Using VR-CESM, Journal of Geophysical Research: Atmospheres, 124, 4490–4513, https://doi.org/10.1029/2018JD028925, 2019.

Rauscher, S. A., Ringler, T. D., Skamarock, W. C., and Mirin, A. A.: Exploring a global multiresolution modeling approach using aquaplanet simulations*, J Clim, 26, https://doi.org/10.1175/JCLI-D-12-00154.1, 2013.

Rhoades, A. M., Huang, X., Ullrich, P. A., and Zarzycki, C. M.: Characterizing Sierra Nevada Snowpack Using Variable-Resolution CESM, J Appl Meteorol Climatol, 55, 173–196, https://doi.org/10.1175/JAMC-D-15-0156.1, 2016.

Rhoades, A. M., Ullrich, P. A., Zarzycki, C. M., Johansen, H., Margulis, S. A., Morrison, H., Xu, Z., and Collins, W. D.: Sensitivity of Mountain Hydroclimate Simulations in Variable-Resolution CESM to Microphysics and Horizontal Resolution, J Adv Model Earth Syst, 10, 1357–1380, https://doi.org/10.1029/2018MS001326, 2018.

Roeckner, E., Brokopf, R., Esch, M., Giorgetta, M. A., Hagemann, S., Kornblueh, L., Manzini, E., Schlese, U., and Schulzweida, U.: Sensitivity of simulated climate to horizontal and vertical resolution in the ECHAM5 atmosphere model, J Clim, 19, https://doi.org/10.1175/JCLI3824.1, 2006.

Sellevold, R., van Kampenhout, L., Lenaerts, J. T. M., Noël, B., Lipscomb, W. H., and Vizcaino, M.: Surface mass balance downscaling through elevation classes in an Earth system model: application to the Greenland ice sheet, Cryosphere, 13, 3193–3208, https://doi.org/10.5194/tc-13-3193-2019, 2019.

Shannon, S., Smith, R., Wiltshire, A., Payne, T., Huss, M., Betts, R., Caesar, J., Koutroulis, A., Jones, D., and Harrison, S.: Global glacier volume projections under high-end climate change scenarios, Cryosphere, 13, 325–350, https://doi.org/10.5194/tc-13-325-2019, 2019.

Shean, D. E., Bhushan, S., Montesano, P., Rounce, D. R., Arendt, A., and Osmanoglu, B.: A Systematic, Regional Assessment of High Mountain Asia Glacier Mass Balance, Front Earth Sci (Lausanne), 7, https://doi.org/10.3389/feart.2019.00363, 2020.

Skamarock, W. C., Park, S. H., Klemp, J. B., and Snyder, C.: Atmospheric kinetic energy spectra from global high-resolution nonhydrostatic simulations, J Atmos Sci, 71, https://doi.org/10.1175/JAS-D-14-0114.1, 2014.

Slater, A. G., Schlosser, C. A., Desborough, C. E., Pitman, A. J., Henderson-Sellers, A., Robock, A., Vinnikov, K. Y., Mitchell, K., Boone, A., Braden, H., Chen, F., Cox, P. M., De Rosnay, P., Dickinson, R. E., Dai, Y. J., Duan, Q., Entin, J., Etchevers, P., Gedney, N., Gusev, Y. M., Habets, F., Kim, J., Koren, V., Kowalczyk, E. A., Nasonova, O. N., Noilhan, J., Schaake, S., Shmakin, A. B., Smirnova, T. G., Verseghy, D., Wetzel, P., Xue, Y., Yang, Z. L., and Zeng, Q.: The representation of snow in land surface schemes: Results from PILPS 2(d), J Hydrometeorol, 2, https://doi.org/10.1175/1525-7541(2001)002<0007:TROSIL>2.0.CO;2, 2001.

Smith, T. and Bookhagen, B.: Changes in seasonal snow water equivalent distribution in High Mountain Asia (1987 to 2009), Sci Adv, 4, e1701550, https://doi.org/10.1126/sciadv.1701550, 2018.

Swenson, S. C., Clark, M., Fan, Y., Lawrence, D. M., and Perket, J.: Representing Intrahillslope Lateral Subsurface Flow in the Community Land Model, J Adv Model Earth Syst, 11, https://doi.org/10.1029/2019MS001833, 2019.

Tesfa, T. K., Leung, L. R., and Ghan, S. J.: Exploring Topography-Based Methods for Downscaling Subgrid Precipitation for Use in Earth System Models, Journal of Geophysical Research: Atmospheres, 125, https://doi.org/10.1029/2019JD031456, 2020.

Van Tricht, K., Lhermitte, S., Gorodetskaya, I. V., and Van Lipzig, N. P. M.: Improving satellite-retrieved surface radiative fluxes in polar regions using a smart sampling approach, Cryosphere, 10, https://doi.org/10.5194/tc-10-2379-2016, 2016.

Viste, E. and Sorteberg, A.: Snowfall in the Himalayas: an uncertain future from a little-known past, Cryosphere, 9, 1147–1167, https://doi.org/10.5194/tc-9-1147-2015, 2015.

Vizcaino, M.: Ice sheets as interactive components of Earth System Models: progress and challenges, Wiley Interdiscip Rev Clim Change, 5, 557–568, https://doi.org/10.1002/wcc.285, 2014.

Vizcaíno, M., Lipscomb, W. H., Sacks, W. J., van Angelen, J. H., Wouters, B., and van den Broeke, M. R.: Greenland Surface Mass Balance as Simulated by the Community Earth System Model. Part I: Model Evaluation and 1850–2005 Results, J Clim, 26, 7793–7812, https://doi.org/10.1175/JCLI-D-12-00615.1, 2013.

Wang, R., Ding, Y., Shangguan, D., Guo, W., Zhao, Q., Li, Y., and Song, M.: Influence of Topographic Shading on the Mass Balance of the High Mountain Asia Glaciers, Remote Sens (Basel), 14, https://doi.org/10.3390/rs14071576, 2022.

Wang, X., Tolksdorf, V., Otto, M., and Scherer, D.: WRF-based dynamical downscaling of ERA5 reanalysis data for High Mountain Asia: Towards a new version of the High Asia Refined analysis, International Journal of Climatology, 41, 743–762, https://doi.org/10.1002/joc.6686, 2021.

Waterman, T., Bragg, A., Simon, J., and Chaney, N.: Capturing the Effects of Surface Heterogeneity Induced Secondary Circulations on the Lower Sub-grid Atmosphere in Earth System Models, in: EGU General Assembly 2022, https://doi.org/10.5194/egusphere-egu22-10646, 2022.

Wedi, N. P. and Smolarkiewicz, P. K.: A framework for testing global non-hydrostatic models, Quarterly Journal of the Royal Meteorological Society, 135, https://doi.org/10.1002/qj.377, 2009.

Weedon, G. P., Balsamo, G., Bellouin, N., Gomes, S., Best, M. J., and Viterbo, P.: The WFDEI meteorological forcing data set: WATCH Forcing data methodology applied to ERA-Interim reanalysis data, Water Resour Res, 50, 7505–7514, https://doi.org/10.1002/2014WR015638, 2014.

Wijngaard, R. R., Lutz, A. F., Nepal, S., Khanal, S., Pradhananga, S., Shrestha, A. B., and Immerzeel, W. W.: Future changes in hydro-climatic extremes in the Upper Indus, Ganges, and Brahmaputra River basins, PLoS One, 12, 26, https://doi.org/10.1371/journal.pone.0190224, 2017.

Wijngaard, R. R., Herrington, A. R., Lipscomb, W. H., Leguy, G. R., and An, S.-I.: CLM/CTSM glacier input datasets used for study on evaluation variable-resolution CESM2 in High-Mountain Asia, https://doi.org/10.5281/ZENODO.7864689, 2023.

Williamson, D. L.: Convergence of aqua-planet simulations with increasing resolution in the Community Atmospheric Model, Version 3, in: Tellus, Series A: Dynamic Meteorology and Oceanography, https://doi.org/10.1111/j.1600-0870.2008.00339.x, 2008.

Wu, X., Reed, K. A., Callaghan, P., and Bacmeister, J. T.: Exploring Western North Pacific Tropical Cyclone Activity in the High-Resolution Community Atmosphere Model, Earth and Space Science, 9, https://doi.org/10.1029/2021EA001862, 2022.

Xu, Z., Di Vittorio, A., Zhang, J., Rhoades, A., Xin, X., Xu, H., and Xiao, C.: Evaluating Variable-Resolution CESM Over China and Western United States for Use in Water-Energy Nexus and Impacts Modeling, Journal of Geophysical Research: Atmospheres, 126, https://doi.org/10.1029/2020JD034361, 2021.

Yang, Q., Leung, L. R., Lu, J., Lin, Y. L., Hagos, S., Sakaguchi, K., and Gao, Y.: Exploring the effects of a nonhydrostatic dynamical core in high-resolution aquaplanet simulations, J Geophys Res, 122, https://doi.org/10.1002/2016JD025287, 2017.

Yao, T., Thompson, L., Yang, W., Yu, W., Gao, Y., Guo, X., Yang, X., Duan, K., Zhao, H., Xu, B., Pu, J., Lu, A., Xiang, Y., Kattel, D. B., and Joswiak, D.: Different glacier status with atmospheric circulations in Tibetan Plateau and surroundings, Nat Clim Chang, 2, 663–667, https://doi.org/10.1038/nclimate1580, 2012.

Zarzycki, C. M., Levy, M. N., Jablonowski, C., Overfelt, J. R., Taylor, M. A., and Ullrich, P. A.: Aquaplanet Experiments Using CAM's Variable-Resolution Dynamical Core, J Clim, 27, 5481–5503, https://doi.org/10.1175/JCLI-D-14-00004.1, 2014.

Zemp, M., Huss, M., Thibert, E., Eckert, N., McNabb, R., Huber, J., Barandun, M., Machguth, H., Nussbaumer, S. U., Gärtner-Roer, I., Thomson, L., Paul, F., Maussion, F., Kutuzov, S., and Cogley, J. G.: Global glacier mass changes and their contributions to sea-level rise from 1961 to 2016, Nature, 568, 382–386, https://doi.org/10.1038/s41586-019-1071-0, 2019.

Zhang, G. J. and McFarlane, N. A.: Sensitivity of climate simulations to the parameterization of cumulus convection in the canadian climate centre general circulation model, Atmosphere - Ocean, 33, https://doi.org/10.1080/07055900.1995.9649539, 1995.

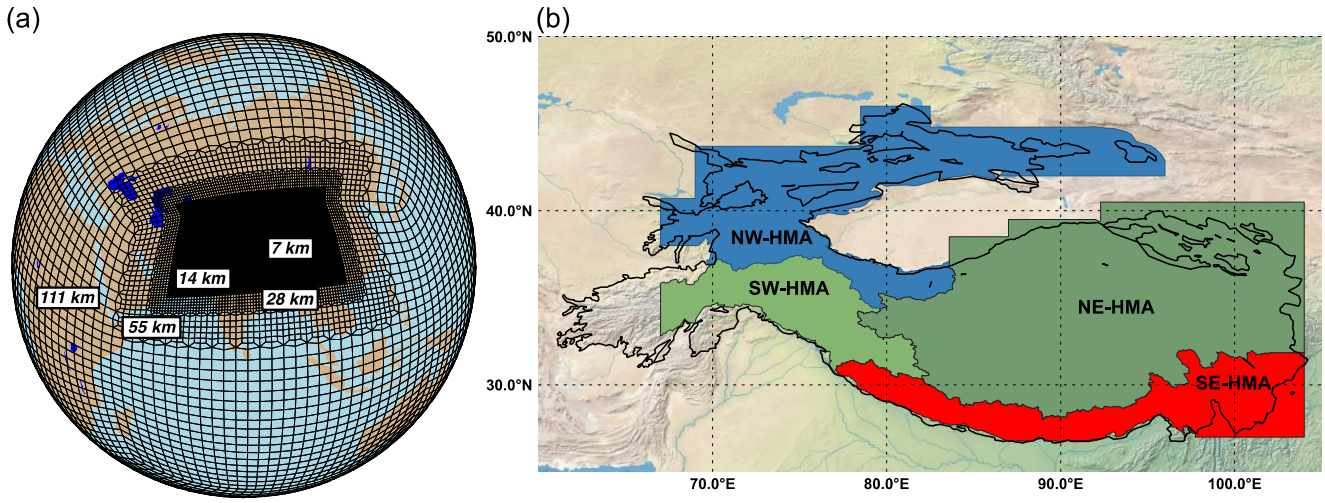

Figure 1. (**a**) Variable-resolution (VR) spectral element (SE) grid developed for this study, and (**b**) map showing High Mountain Asia (HMA) subregions used to evaluate cryospheric-hydrological variables, along with the outline of HMA. The source of the background imagery in Figure 1b is http://naturalearthdata.com/ (last access: 12 April 2022). The HMA subregions are derived from Randolph Glacier Inventory (RGI) version 6 regions (RGI Consortium, 2017), where SW-HMA and SE-HMA represent RGI regions South Asia West and South Asia East, respectively, and NW-HMA and NE-HMA represent RGI region Central Asia. Central Asia has been split into two subregions to better represent the regional climate characteristics. The HMA outline is derived from the Global Mountain Biodiversity Assessment (GMBA) Mountain Inventory version 1.2 (Körner et al., 2017).

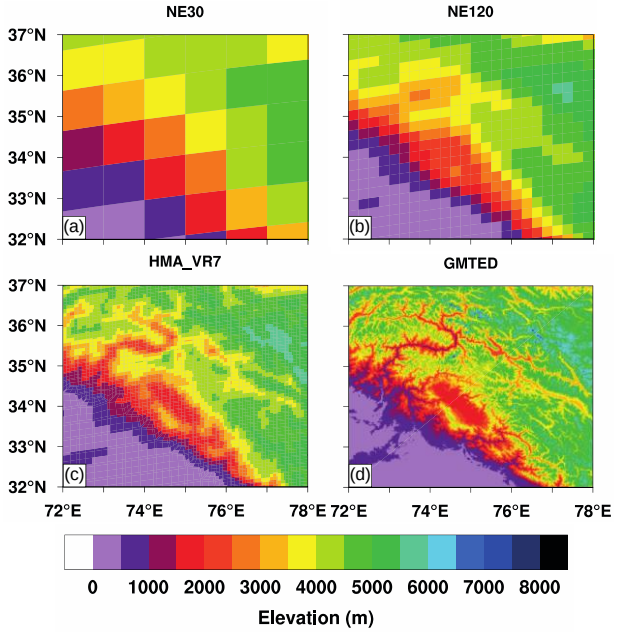

Figure 2. Topographical representation of western High Mountain Asia (i.e., Upper Indus River and Karakoram Mountains, 32°–37° N; 72°–78° E) by globally uniform 1° and 0.25° CESM grids (NE30 and NE120, respectively) (**a-b**), the HMA_VR7 grid (**c**), and a reference dataset, GMTED2010 (Danielson and Gesch, 2011) (**d**).

Table 1. Maximum altitude per HMA subregion (Figure 1b) as observed for NE30, NE120, HMA_VR7 and GMTED2010.

	NW-HMA	NE-HMA	SW-HMA	SE-HMA
NE30	5162 m	5170 m	4978 m	4452 m
NE120	5684 m	5526 m	5513 m	5369 m
HMA_VR7	6167 m	5778 m	5870 m	6228 m
GMTED2010	7325 m	7099 m	8190 m	8625 m

Table 2~~1~~. Overview of the modelling setup differences between the first and second HMA VR simulations (HMA-VR7a and HMA-VR7b, respectively).

	Simulation 1 (HMA_VR7a)	**Simulation 2 (HMA_VR7b)**
Spin-up length	1 year	10 years for atmospheric component 50 years for land surface component
Snow depth (m w.e.)	1 m w.e.	5 m w.e.
Bare ice albedo visible (near-infrared)	0.5 (0.3)	0.6 (0.4)
Longwave downscaling	Yes	No
Rain-snow temperature thresholds snow (rain)	-2 °C (0 °C) for glacier land units 0 °C (+2 °C) for non-glacier land units	0 °C (+4 °C)
Glacier-cover dataset	Default	Updated
Other tunings		Tunings on cloud cover and sea ice + MG3 cloud microphysics scheme

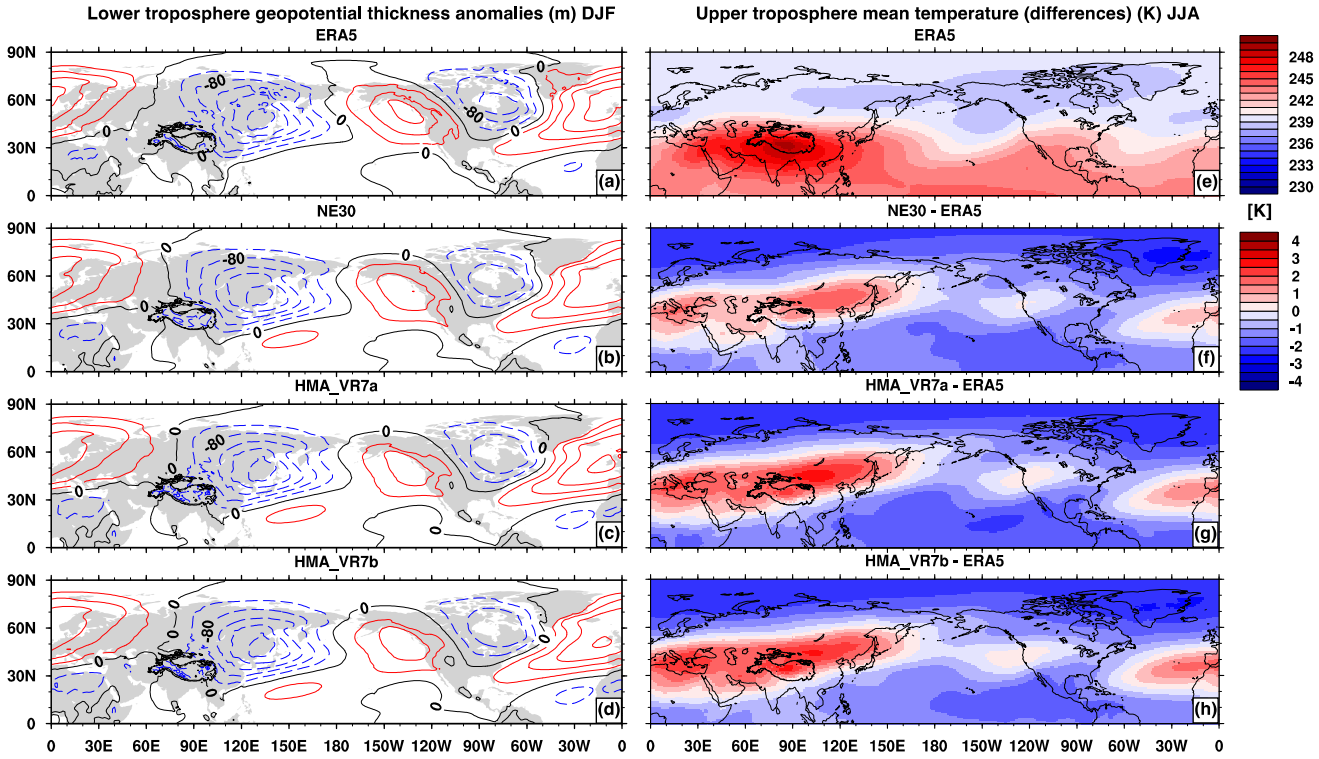

Figure 3. (**a-d**) Northern Hemisphere, lower troposphere eddy of the 500–1000 hPa geopotential thickness (m) in winter (DJF) for ERA5 (**a**), NE30 (**b**), HMA_VR7a (**c**), and HMA_VR7b (**d**). (**e-h**) Northern Hemisphere, upper troposphere (200–500 hPa) summer (JJA) mean temperature (K) for ERA5 (**e**), and the ~~absolute~~ temperature differences relative to ERA5 for NE30 (**f**), HMA_VR7a (**g**), and HMA_VR7b (**h**).

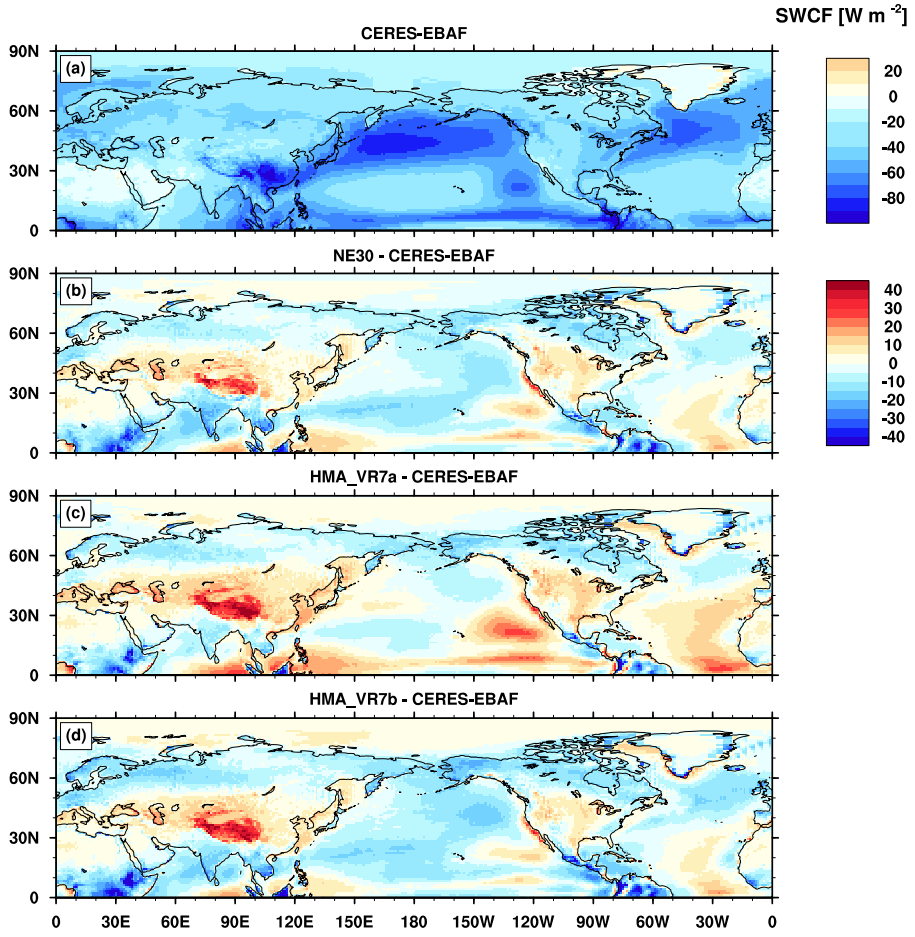

Figure 4. Northern Hemisphere annual mean shortwave cloud forcing (W m^{-2}) from CERES-EBAF (**a**) and model biases relative to CERES-EBAF (**b-d**) for NE30 (**b**), HMA_VR7a (**c**), and HMA_VR7b (**d**). All differences are computed after mapping model fields to the CERES-EBAF 1˚ grid.

980

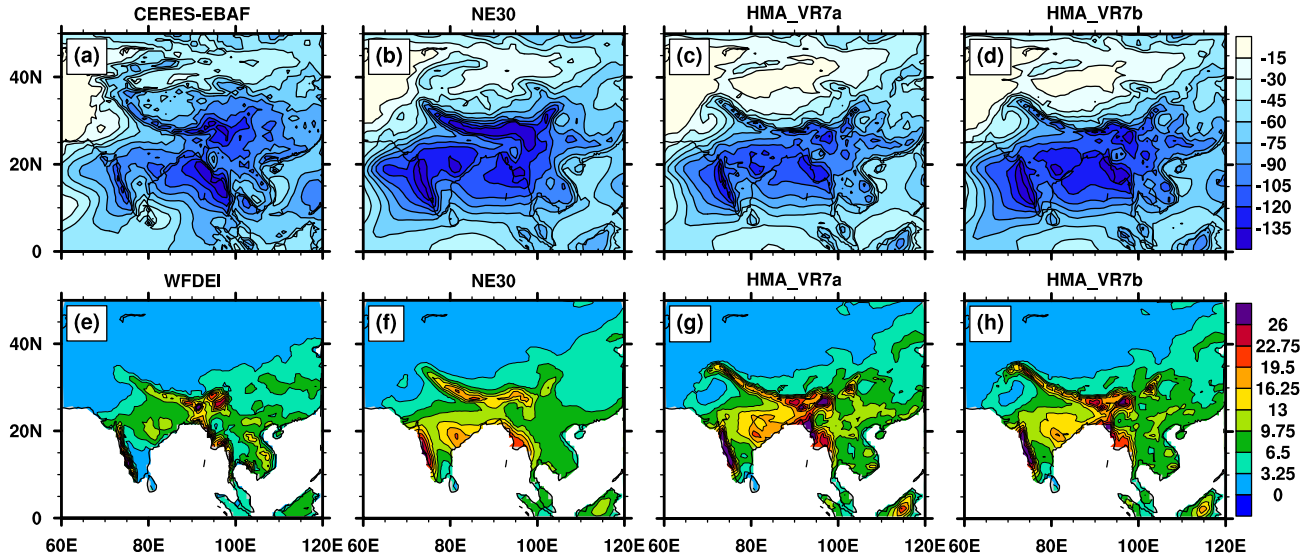

Figure 5. Northern Hemisphere summer climatological (**a-d**) shortwave cloud forcing (W m^{-2}) and (**e-h**) precipitation rate (mm/day) in observations and models. (**a**) CERES-EBAF, (**b,f**) NE30, (**c,g**) HMA_VR7a, (**d,h**) HMA_VR7b, and (**e**) WFDEI precipitation rates. Top panels show fields mapped to the CERES-EBAF 1˚ grid, and the bottom panels show fields mapped to the NE30 grid.

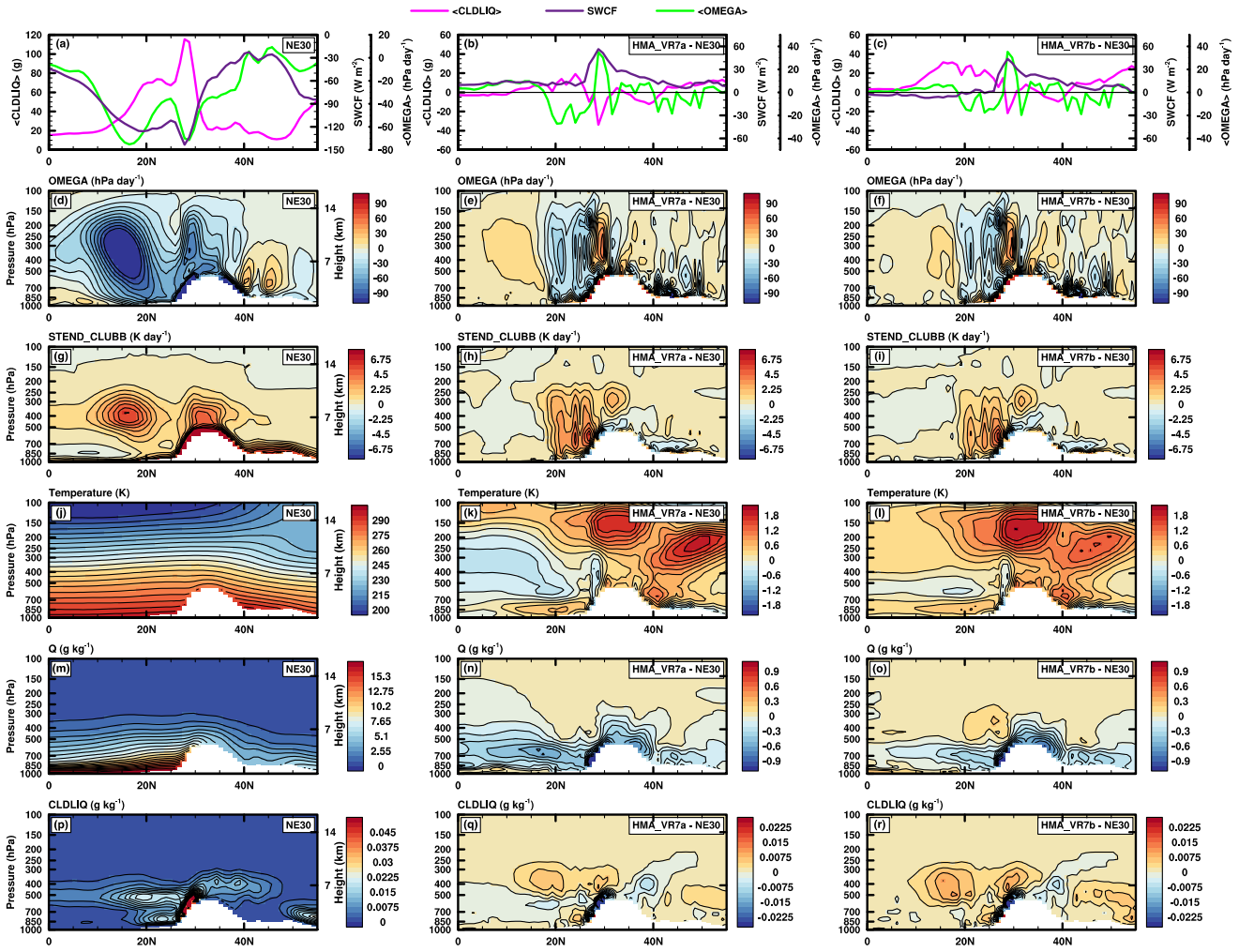

Figure 6. Northern Hemisphere summer climatological mass fraction of cloud liquid amount (CLDLIQ, g kg^{-1}), shortwave cloud forcing (SWCF, W m^{-2}), vertical velocity (OMEGA, hPa day^{-1}), CLUBB condensational heating (STEND_CLUBB, K day^{-1}), air temperature (K), and specific humidity (Q, g kg^{-1}) in a latitude-height transect averaged over 80°–100° longitude. (Left column) NE30, (middle column) HMA_VR7a differences relative to NE30, (right column) HMA_VR7b differences relative to NE30.

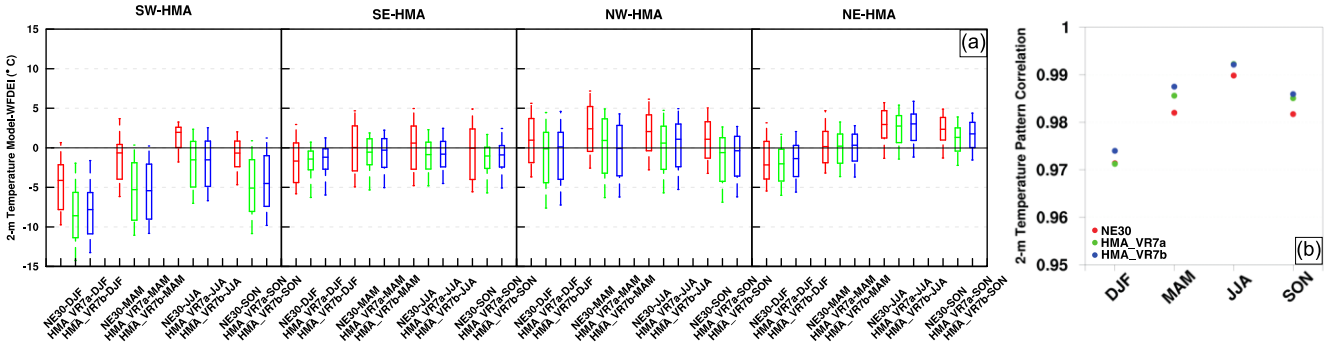

Figure 7. (**a**) Boxplots of ~~absolute~~ 2-m temperature differences (°C) between the simulation outputs of NE30 (red), HMA_VR7a (green), HMA_VR7b (blue), and the observation/reanalysis-based WFDEI for each season and HMA subregion (shown in Figure 1b). The box represents the biases between the 25th and 75th percentile, the line in the box denotes the median, and the whiskers represent the 10th ~~minimum~~ and 90th percentile of ~~maximum absolute~~ temperature differences. (**b**) Pattern correlations between the simulation outputs of NE30 (red), HMA_VR7a (green), HMA_VR7b (blue), and the observation/reanalysis-based WFDEI. The pattern correlations are calculated for each season and for the entire HMA region.

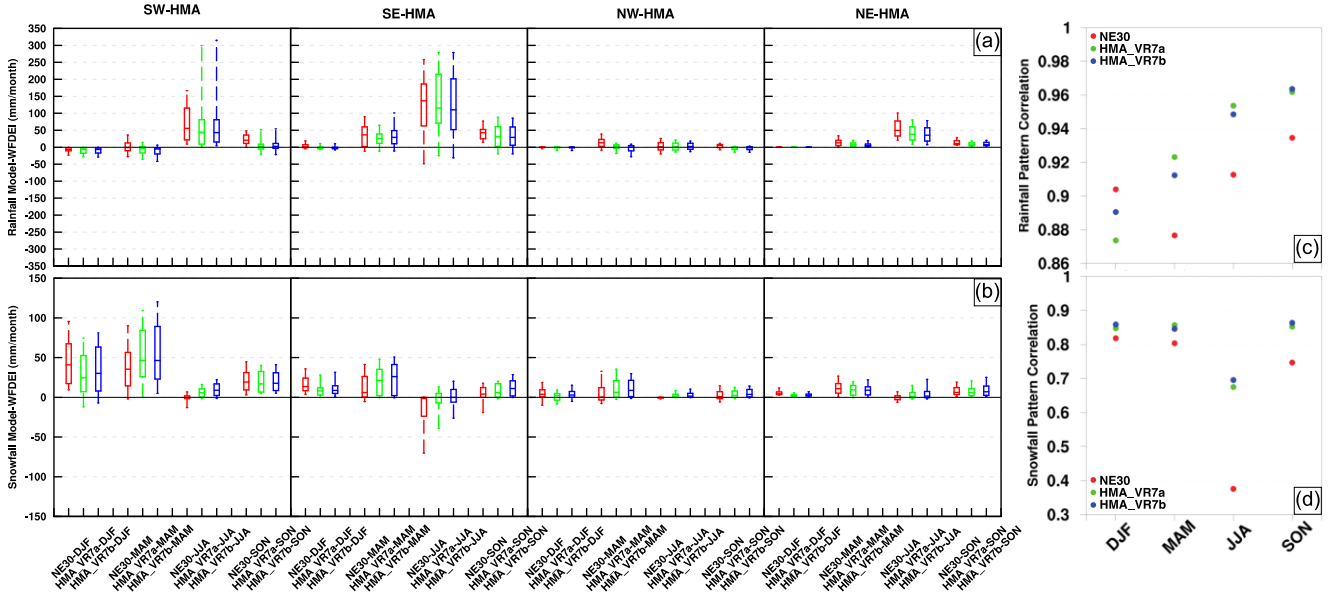

Figure 8. Same as Figure 7, but for rainfall (mm month^{-1}) (**a-**~~**c**~~**b**) and snowfall (mm month^{-1}) (**b**~~**c**~~**-d**)

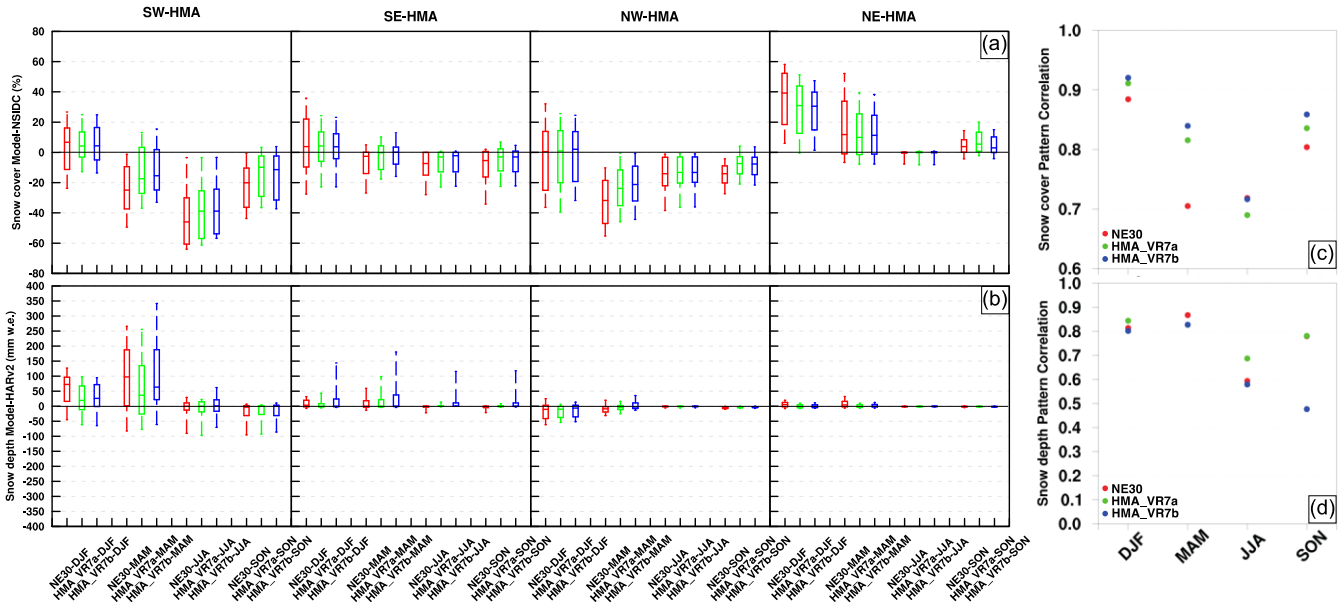

Figure 9. Same as Figure 7, but for snow cover (%) (**a-b**) and snow depth (mm w.e.) (**c-d**). The ~~absolute~~ snow cover and snow depth differences are calculated between CESM simulation output (i.e., NE30, HMA_V7a and HMA_VR7b) and snow cover derived from NSIDC, and snow depth derived from HARv2~~JRA55~~, respectively.

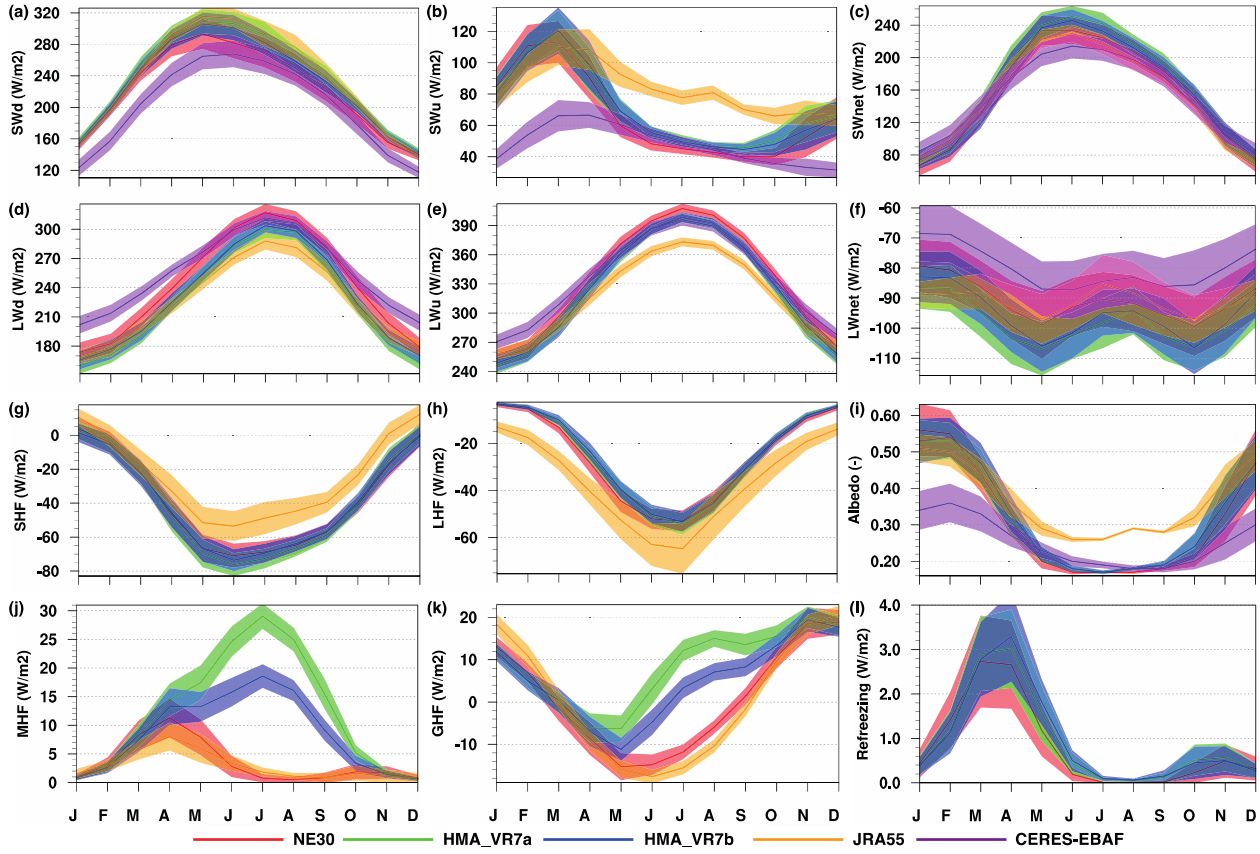

Figure 10. Annual cycle of (**a**) downwelling shortwave radiation (SW_d), (**b**) upwelling shortwave radiation (SW_u), (**c**) net shortwave radiation (SW_{net}), (**d**) downwelling longwave radiation (LW_d), (**e**) upwelling longwave radiation (LW_u), (**f**) net longwave radiation (LW_{net}), (**g**) sensible heat flux (SHF), (**h**) latent heat flux (LHF), (**i**) albedo, (**j**) melt heat flux (MHF), (**k**) conductive/ground heat flux (GHF), and (**l**) refreezing heat flux. The annual cycle of the various SEB fluxes (W m^{-2}) is representative for glaciated grid cells (encompassing all land units) in HMA over the periods 1979–1998 for NE30 (red), HMA_VR7a (green), HMA_VR7b (blue) and JRA55 (orange), and 2001–2020 for CERES-EBAF (purple). The shading denotes the standard deviation in time and SEB fluxes are defined positive towards the surface.

Table 3~~2~~. Mean annual (ANN), wintertime (DJF|, in *italic*), and summertime (JJA, in *italic*) surface-energy-balance (SEB) fluxes (W m^{-2}) for NE30, HMA_VR7a (HMA1), HMA_VR7b (HMA2), JRA55 and CERES-EBAF (C-EBF). SEB fluxes are defined positive towards the surface and represent the mean fluxes in glaciated grid cells (encompassing all land units), averaged over the entire HMA region and the periods 1979–1998 (for NE30, HMA_VR7a, HMA_VR7b, and JRA55) and 2001–2020 (for CERES-EBAF).

SEB fluxes (W m^{-2})	ANN					*DJF|JJA*				
	NE30	HMA1	HMA2	JRA55	C-EBF	*NE30*	*HMA1*	*HMA2*	*JRA55*	*C-EBF*
SW_d	223	236	231	236	201	*162|267*	*168|287*	*164|281*	*162|295*	*133|256*
SW_u	66	71	70	83	48	*87|45*	*85|51*	*83|50*	*80|81*	*42|49*
SW_{net}	157	165	161	153	153	*75|222*	*83|236*	*80|230*	*81|214*	*92|207*
LW_d	242	226	230	225	255	*179|309*	*165|293*	*171|296*	*175|280*	*207|306*
LW_u	333	324	325	316	335	*261|401*	*253|392*	*256|393*	*263|369*	*277|391*
LW_{net}	-91	-98	-95	-91	-80	*-82|-92*	*-88|-98*	*-85|-97*	*-89|-89*	*-71|-85*
R_{net}	66	67	66	62	73	*-7|130*	*-5|138*	*-5|133*	*-8|125*	*21|122*
SHF	-38	-39	-38	-24	-	*~0|-68*	*-0.5|-72*	*-2|-69*	*7|-49*	-
LHF	-26	-25	-24	-36	-	*-5|-50*	*-4|-50*	*-4|-50*	*-14|-60*	-
GHF	1	9	5	1	-	*13|-11*	*12|10*	*12|2*	*16|-15*	-
MHF	3	12	9	3	-	*2|1*	*2|26*	*2|17*	*2|2*	-
Refreezing	0.81	0.92	0.95	-	-	*0.7|0.07*	*0.6|0.19*	*0.6|0.22*	-	-

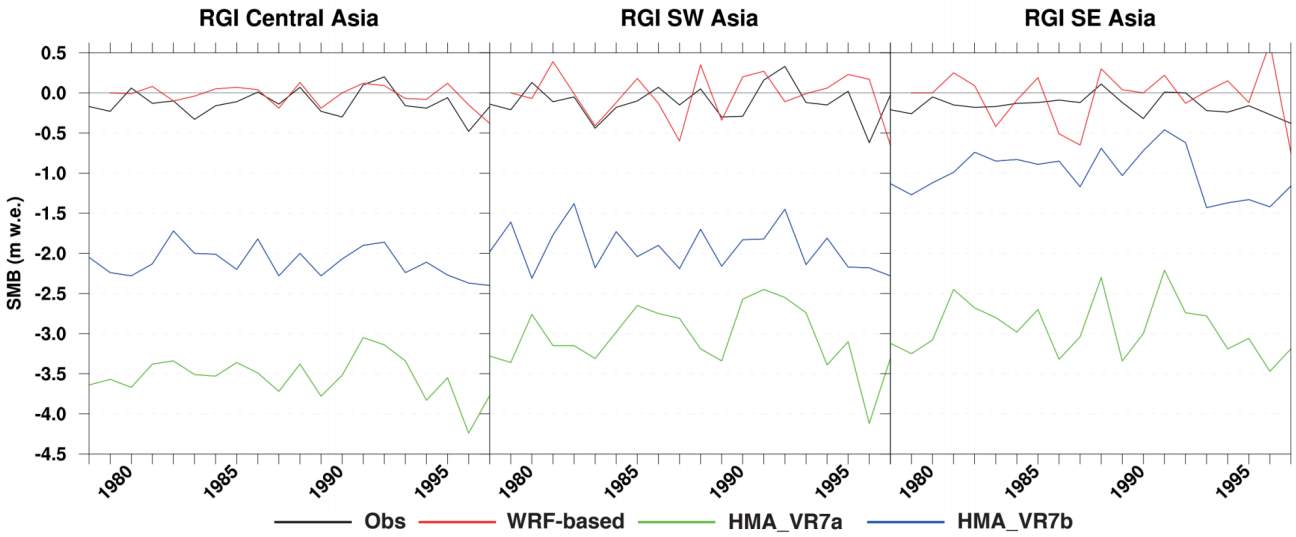

Figure 11. Area-averaged annual SMB (m w.e. yr^{-1}) over the period 1979–1998 derived from geodetical and glaciological observations (Zemp et al., 2019) (Obs, blackue), gridded outputs from a glacier model forced by WRF output (de Kok et al., 2020) (WRF-based, red), and simulation outputs of HMA_VR7a (green) and HMA_VR7b (blue). The area-averaged annual SMB is calculated for three different regions: RGI region Central Asia, which includes the HMA subregions NW-HMA and NE-HMA (Figure 1), and RGI regions SW Asia and SE Asia, which represent HMA subregions SW-HMA and SE-HMA, respectively (Figure 1).

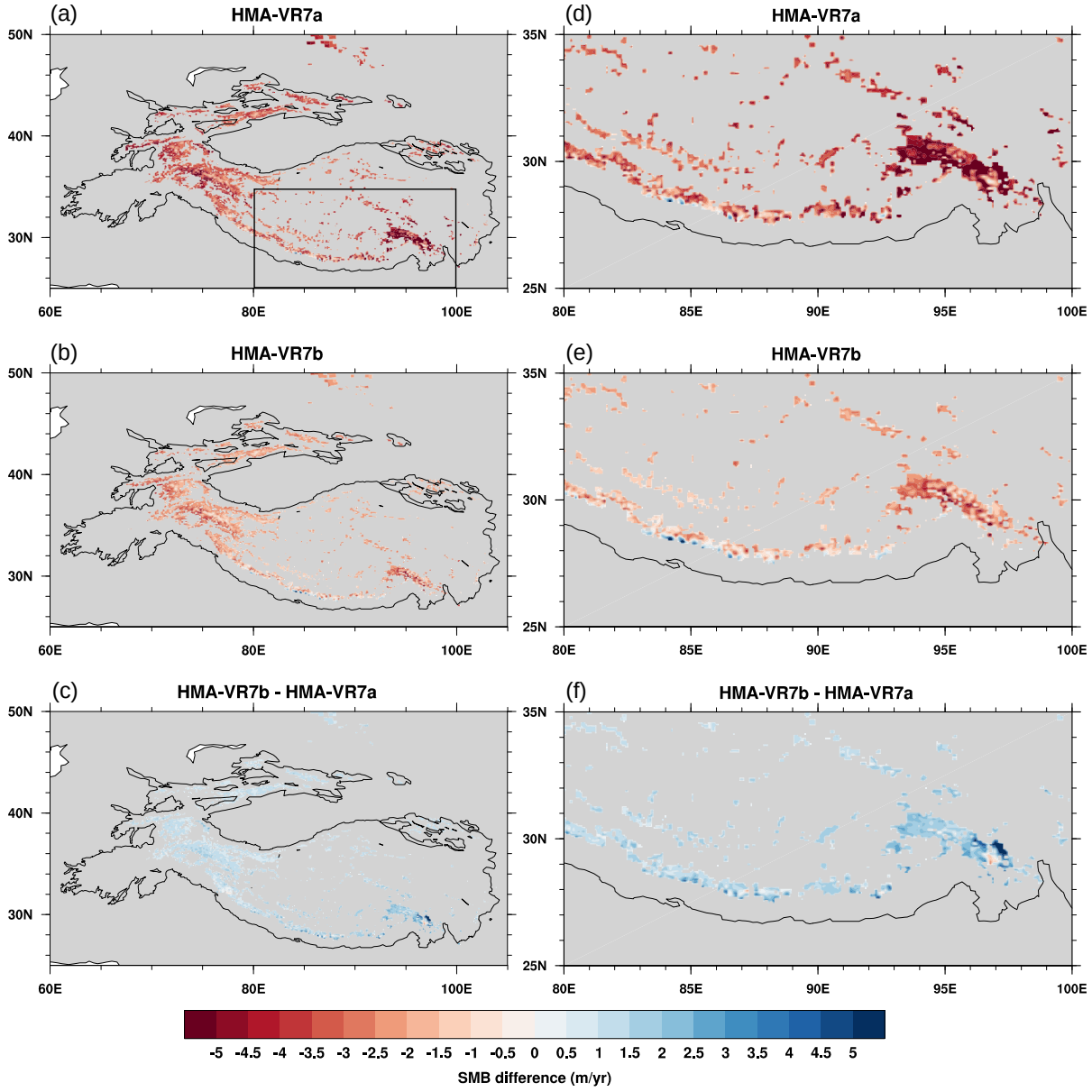

Figure 12. Spatial distribution of mean annual SMB (m w.e. yr^{-1}) over the period 1979–1998 as simulated by HMA_VR7a (**a-b**) and HMA-VR7b (**c-d**), and the SMB differences between the two simulations (**e-f**). The black box in Figure 124a denote the area (25°–35°N; 80°–100°E) of the insets over southeastern HMA (**d, e, f**). The HMA outline is derived from the Global Mountain Biodiversity Assessment (GMBA) Mountain Inventory version 1.2 (Körner et al., 2017).

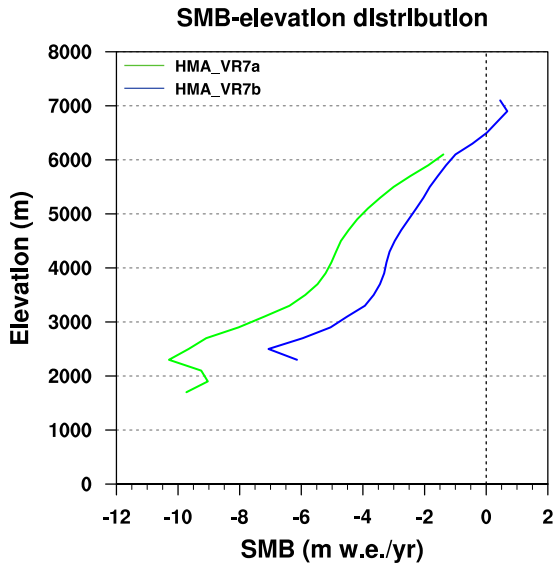

Figure 13. Mean elevation profile of glacier SMB (m w.e. yr^{-1}) over HMA for the period 1979–1998. The green and blue lines denote the SMB-elevation profiles for HMA_VR7a and HMA_VR7b, respectively.

Table 43. Mean integrated SMB mass fluxes (Gt yr^{-1}) for the period 1979–1998 in gigatons per year. The numbers in brackets denote the standard deviation in time. The integrated SMB mass fluxes have been calculated over two different areas of integration for HMA_VR7a, derived from the original and updated glacier-cover datasets, respectively. The SMB mass fluxes for HMA_VR7a that are integrated over the glacier areas of the updated glacier-cover dataset are denoted as HMA_VR7a_GC2. The mass fluxes of HMA_VR7b are only integrated over the glacier areas of the updated dataset.

Simulation	Glacier Area (km^2)	Precipitation (Gt yr^{-1})	Ice Melt (Gt yr^{-1})	Total Melt (Gt yr^{-1})	Refreezing (Gt yr^{-1})	Runoff (Gt yr^{-1})	Sublimation/ Evaporation (Gt yr^{-1})	SMB (Gt yr^{-1})
HMA_VR7a	120,087	111 (6)	463 (33)	553 (29)	34 (2)	554 (33)	15 (1)	-459 (33)
HMA_VR7a_GC2	96,493	90 (5)	356 (26)	432 (23)	29 (2)	430 (26)	12 (0.6)	-352 (27)
HMA_VR7b	96,493	93 (4)	228 (20)	324 (18)	32 (2)	306 (21)	12 (0.5)	-224 (21)

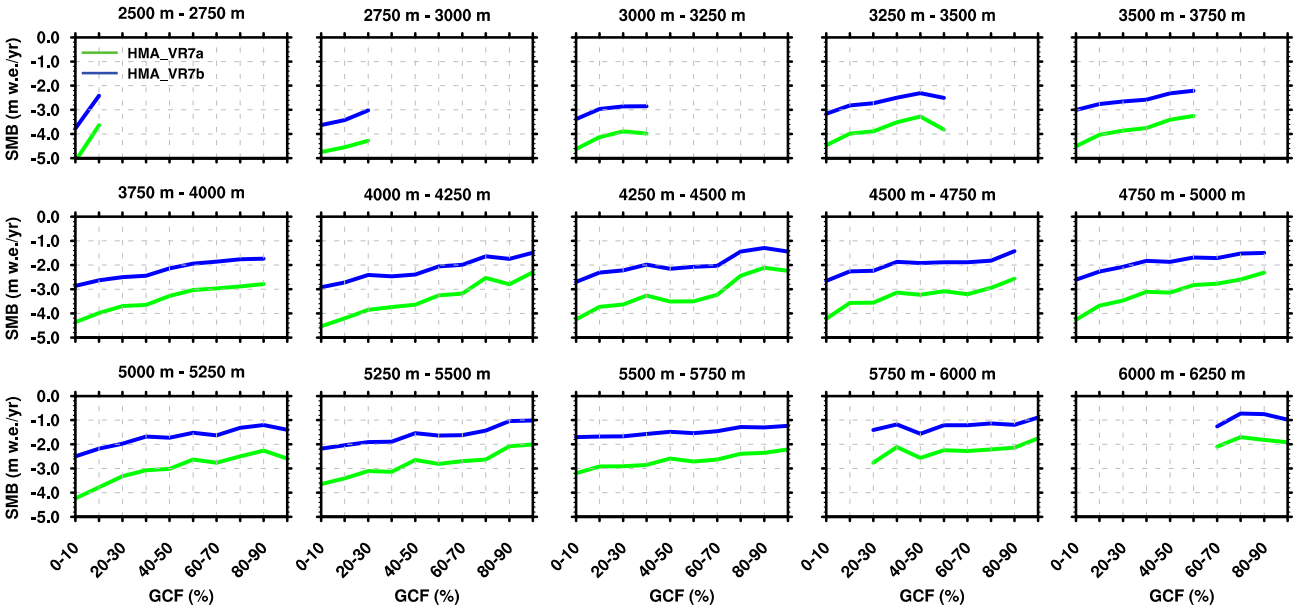

Figure 14. CLM grid-cell-mean SMB-glacier fraction distributions for HMA_VR7a (green) and HMA_VR7b (blue). The SMB–glacier elevation distributions are calculated for 15 different 250m elevation zones between 2500 m and 6250 m altitude, where elevation zones are based on CLM grid-cell-mean elevation distributions.

Supplement of

Exploring the ability of the variable-resolution CESM to simulate cryospheric-hydrological variables in High Mountain Asia

René R. Wijngaard[1,*], Adam R. Herrington[2], William H. Lipscomb[2], Gunter R. Leguy[2], and Soon-Il An[1,3]

[1]Irreversible Climate Change Research Center, Yonsei University, Seoul, South Korea
[2]Climate and Global Dynamics Laboratory, National Center for Atmospheric Research, Boulder CO, USA
[3]Climate Theory Lab, Department of Atmospheric Sciences, Yonsei University, Seoul, South Korea
[*]Now at: Institute for Marine and Atmospheric Research Utrecht, Utrecht University, Utrecht, the Netherlands

Correspondence to: Soon-Il An (sian@yonsei.ac.kr) and René R. Wijngaard (r.r.wijngaard.uu@gmail.com)

Section S1 CLM Glacier-Cover Dataset

For the HMA_VR7b simulation, we updated the CLM glacier-cover dataset to represent glacier and ice sheet cover more accurately. In the original dataset, we found large deviations in parts of HMA between the mean CLM grid cell elevation and the mean glacier elevation derived from the glacier-cover dataset (Figure S1a). These deviations, which were largest in southeastern HMA, are mainly attributable to inaccuracies of the Randolph Glacier Inventory (RGI) version 1 (RGI-Consortium, 2012) glacier outlines used to create the original dataset (Figure S1b).

The updated glacier-cover dataset encompasses three 3-minute datasets: 1) fractional land ice coverage, including both glaciers and ice sheets, 2) distributions of areal glacier coverage by elevation, and 3) distributions of areal ice-sheet coverage by elevation. Figure S2 summarizes the workflow to generate the updated dataset. The fractional land ice coverage and distributions by elevation are derived from global glacier outlines, vector data of ice-sheet coverage, and a global 30-arcsec elevation dataset and land-sea mask. The global glacier outlines are retrieved from the Randolph Glacier Inventory version 6 (RGI-Consortium, 2017), and the vector data for the Greenland and Antarctic ice sheets are retrieved from the masks of BedMachine version 4 (Morlighem et al., 2017, 2021) and version 2 (Morlighem et al., 2020; Morlighem, 2020), respectively. The global elevation data and land-sea mask are obtained from a merged BedMachine/GMTED2010 product in which the higher-resolution BedMachine datasets are conservatively regridded to the 30-arcsec GMTED2010 grid, overwriting the GMTED2010 Greenland and Antarctica values. First, 30-arcsec polygon grids are generated, which are overlaid with global glacier outlines and ice-sheet vector data, respectively, to calculate ice percent cover in each polygon grid cell. The polygon grid cells are then concatenated, followed by the rasterization of the polygon grids. This results in two 30-arcsec land ice masks containing fractional ice coverage for glaciers and ice sheets, respectively. Second, the land ice masks are draped over global

30-arcsec elevation data. In each grid cell, ice fractions are distributed over 70 elevation bins (at 100 m intervals) and an additional bin that includes ice cover above 7000 m, resulting in 30-arcsec distributions of areal ice coverage by elevation for glaciers and ice sheets. Third, the elevation distributions are conservatively regridded to 3-minute resolution and aggregated to generate 3-minute distributions of fractional land ice coverage. Finally, the land-sea mask is conservatively regridded to 3-minute resolution and is corrected by defining grid cells as land where ice cover (including floating ice shelves) is present.

Given the new CLM surface datasets, the distributions by elevation are used to subdivide each CLM glacier land unit into columns based on the 36 ECs defined above. More detailed information about the original glacier-cover dataset can be found in the CLM5 Documentation (https://escomp.github.io/ctsm-docs/). Differences between the original and updated datasets are listed in Table S1.

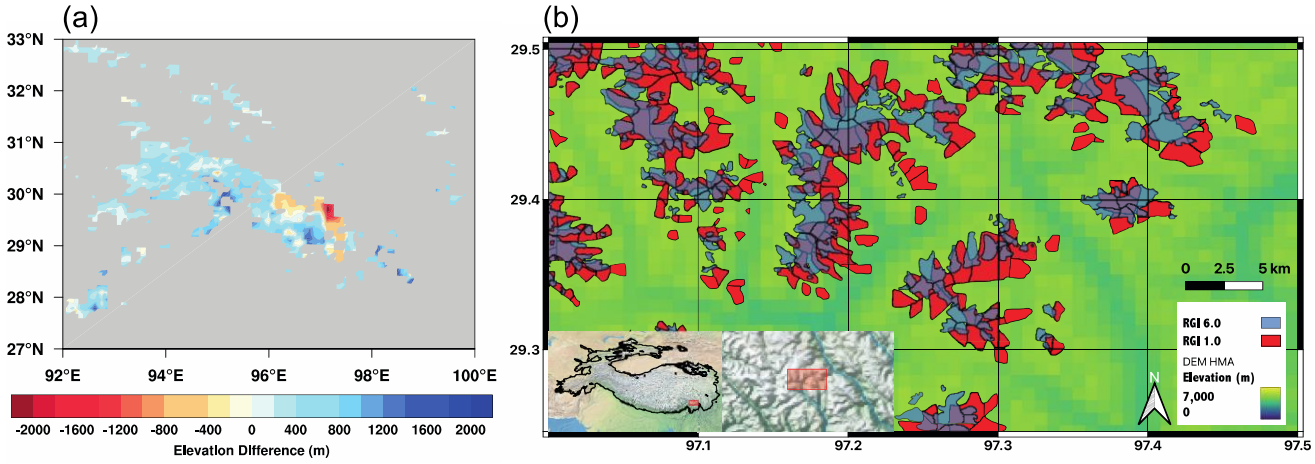

Figure S1. (**a**) Differences between the mean elevation of the CLM grid cell and the mean glacier elevation within the grid cell. (**b**) Glacier outlines retrieved from Randolph Glacier Inventory version 1 (red) and version 6 (blue) (RGI-Consortium, 2012, 2017). The background elevation data is retrieved from Natural Earth. The red box in the insets denote the location of the glacier outlines and the black outline represents the ~~in the insets denote the location of the glacier outlines and the~~ outline of High Mountain Asia~~, respectively~~, where the HMA outlines are retrieved from the Global Mountain Biodiversity Assessment (GMBA) Mountain Inventory version 1.2 (Körner et al., 2017). The location of the red box is based on the large negative elevation differences in Figure S1a.

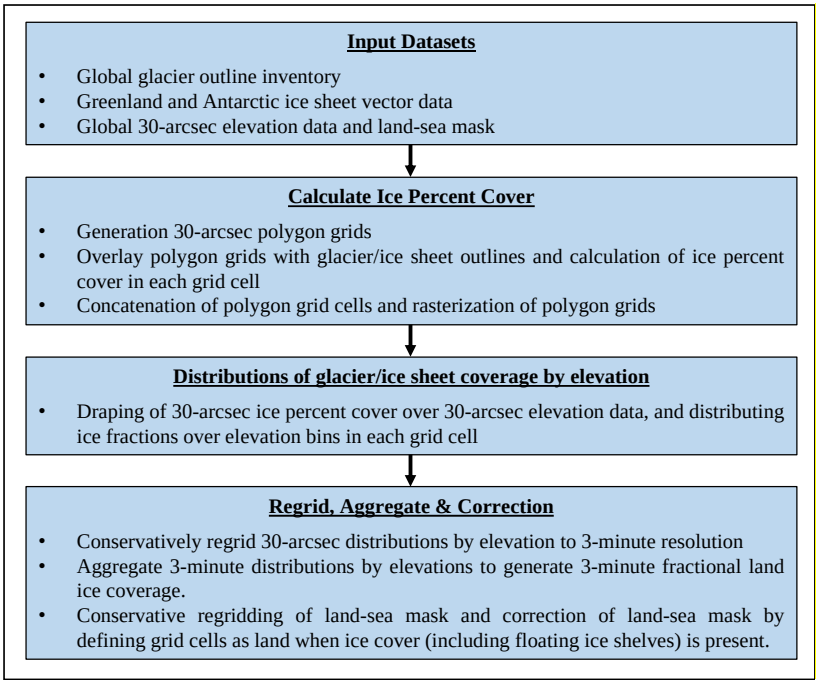

Figure S2. Schematic overview of workflow used for generating the updated CLM glacier-cover dataset.

Table S1. Overview of the input datasets that have been used for the original (v1) and updated (v2) CLM glacier-cover datasets, and the differences in the number of elevation bins that are used among the different glacier-cover datasets.

	CLM glacier-cover dataset v1	**CLM glacier-cover dataset v2**
Glacier outlines	Randolph Glacier Inventory v1 (RGI-Consortium, 2012)	Randolph Glacier Inventory v6 (RGI-Consortium, 2017)
Greenland ice sheet outlines	University of Zurich Raster Data (Rastner et al., 2012)	BedMachine v4 (Morlighem et al., 2017, 2021)
Antarctica ice sheet outlines	SCAR Antarctic Digital Database v5 (ADD Consortium, 2000; Fox et al., 1994)	BedMachine v2 (Morlighem et al., 2020; Morlighem, 2020)
Topography	GLOBE Topography (Hastings et al., 1999)	GMTED2010 (glaciers) + BedMachine (icesheets) (Morlighem et al., 2017, 2020; Danielson and Gesch, 2011)
No. of elevation bins (100 m interval)	60 (< 6000 m) + 1 (6000 – 10,000 m)	70 (< 7000 m) + 1 (7000 – 10,000 m)

Section S2 Supplementary Figures and Tables

Table S2. Mean winter (DJF) and summer (JJA) 2m temperature, rainfall, snowfall, snow cover, and snow depth for NE30, HMA_VR7a, HMA_VR7b, WFDEI (temperature + precipitation), NSIDC (snow cover), and HARv2 (snow depth). The seasonal means/sums are calculated over the HMA subregions (Figure 1b) for the period 1979–1998 (1980 –1998 for HARv2).

	SW-HMA		SE-HMA		NW-HMA		NE-HMA	
2m Temperature (°C)	**DJF**	**JJA**	**DJF**	**JJA**	**DJF**	**JJA**	**DJF**	**JJA**
NE30	-12	13	-1	15	-9	18	-14	12
HMA_VR7a	-16	10	-2	14	-11	16	-14	12
HMA_VR7b	-15	10	-1	14	-11	17	-14	12
WFDEI	-8	12	0	15	-10	16	-12	10
Rainfall (mm)	**DJF**	**JJA**	**DJF**	**JJA**	**DJF**	**JJA**	**DJF**	**JJA**
NE30	25	383	52	1109	14	84	1	342
HMA_VR7a	21	420	37	1171	11	82	0.4	290
HMA_VR7b	19	435	37	1130	11	84	0.3	281
WFDEI	48	145	38	740	16	75	1	163
Snowfall (mm)	**DJF**	**JJA**	**DJF**	**JJA**	**DJF**	**JJA**	**DJF**	**JJA**
NE30	237	9	76	4	62	2	30	20
HMA_VR7a	193	33	58	41	50	12	17	34
HMA_VR7b	208	43	62	53	61	14	19	39
WFDEI	99	12	23	50	45	3	9	18
Snow Cover (%)	**DJF**	**JJA**	**DJF**	**JJA**	**DJF**	**JJA**	**DJF**	**JJA**
NE30	81	2	30	0.1	66	0.2	61	0.2
HMA_VR7a	83	5	28	2	65	1	53	1
HMA_VR7b	83	7	28	2	67	1	52	1
NSIDC	75	42	24	9	68	17	25	2
Snow Depth (mm w.e.)	**DJF**	**JJA**	**DJF**	**JJA**	**DJF**	**JJA**	**DJF**	**JJA**
NE30	157	27	26	0.6	42	2	22	0.2
HMA_VR7a	121	24	27	8	38	1	15	0.4
HMA_VR7b	130	39	50	28	43	2	16	1
HARv2	96	34	17	5	57	4	14	1

Table S3. Mean integrated SMB mass fluxes (Gt yr^{-1}) for the period 1979–1998 (1979–1981 for HMALO simulations) in gigatons per year. The numbers in brackets denote the standard deviation in time. The integrated SMB mass fluxes have been calculated over two different areas of integration for HMA_VR7a, derived from the original and updated glacier-cover datasets, respectively. The SMB mass fluxes for HMA_VR7a (HMALOa) that are integrated over the glacier areas of the updated glacier-cover dataset are denoted as HMA_VR7a_GC2 (HMALOa_GC2). The mass fluxes of HMA_VR7b (HMALOb) are only integrated over the glacier areas of the updated dataset.

Simulation	Glacier	Precipitation	Ice Melt	Total	Refreezing	Runoff	Sublimation/	SMB
HMA_VR7a	120,087	111 (6)	463 (33)	553 (29)	34 (2)	554 (33)	15 (1)	-459
HMA_VR7a_GC2	96,493	90 (5)	356 (26)	432 (23)	29 (2)	430 (26)	12 (0.6)	-352
HMA_VR7b	96,493	93 (4)	228 (20)	324 (18)	32 (2)	306 (21)	12 (0.5)	-224
HMALOa_GC2	96,493	47 (2)	463 (14)	501 (9)	13 (2)	492 (12)	19 (1.0)	-464
HMALOb	96,493	46 (2)	333 (19)	385 (8)	16 (5)	367 (12)	19 (0.9)	-339

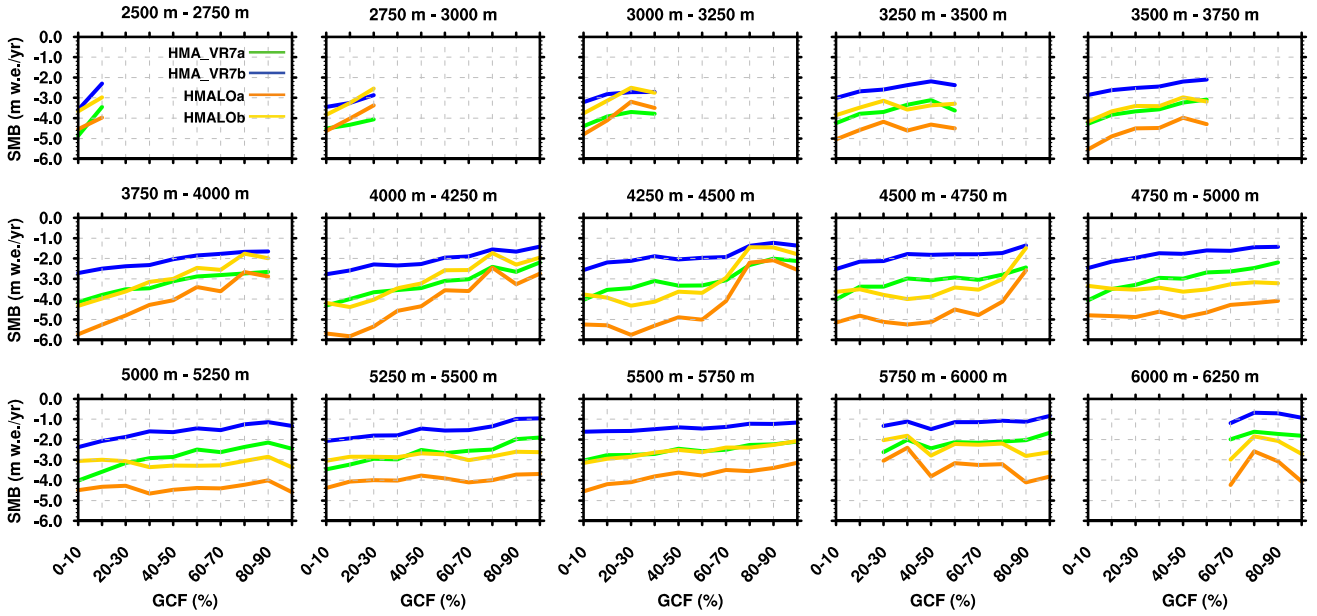

Figure S3. CLM grid-cell-mean SMB-glacier fraction distributions for HMALOa (orange), HMALOb (yellow) HMA_VR7a (green), and HMA_VR7b (blue). The SMB–glacier elevation distributions are calculated for 15 different 250m elevation zones between 2500 m and 6250 m altitude, where elevation zones are based on CLM grid-cell-mean elevation distributions.

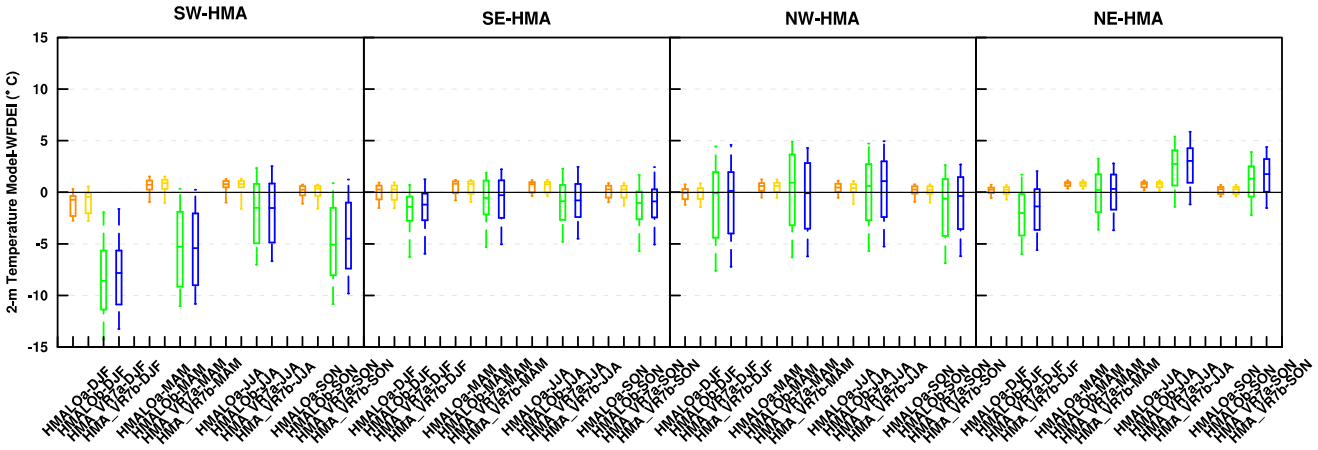

Figure S4. Boxplots of 2-m temperature differences (°C) between the simulation outputs of HMALOa (orange), HMALOb (yellow), HMA_VR7a (green), HMA_VR7b (blue), and the observation/reanalysis-based WFDEI for each season and HMA subregion (shown in Figure 1b). The box represents the biases between the 25th and 75th percentile, the line in the box denotes the median, and the whiskers represent the 10th and 90th percentile of temperature differences.

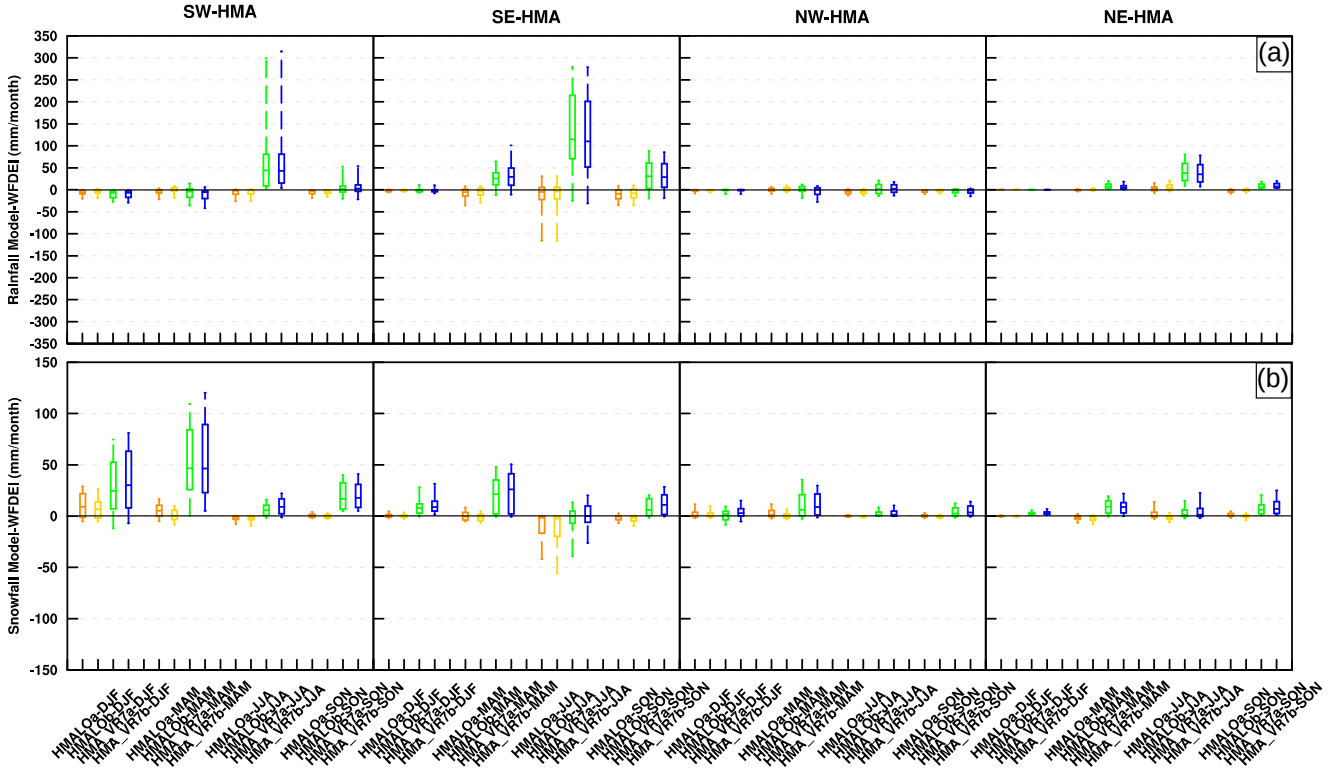

Figure S5. Same as Figure RC1.1, but for rainfall (mm month^{-1}) (**a**) and snowfall (mm month^{-1}) (**b**)

References

ADD Consortium: Antarctic Digital Database, Version 3.0, database, manual and bibliography, Cambridge, 2000.

Danielson, J. J. and Gesch, D. B.: Global Multi-resolution Terrain Elevation Data 2010 (GMTED2010), U.S. Geological Survey Open-File Report 2011-1073, 2011.

Fox, A. J., Paul, A., and Cooper, R.: Measured Properties of the Antarctic Ice Sheet Derived from the Scar Antarctic Digital Database, Polar Record, 30, https://doi.org/10.1017/S0032247400024268, 1994.

Hastings, D. A., Dunbar, P. K., Elphingstone, G. M., Bootz, M., Murakami, H., Maruyama, H., Masaharu, H., Holland, P., Payne, J., Bryant, N. A., Logan, T. L., Muller, J.-P., Schreier, G., and MacDonald, J. S.: The Global Land One-kilometer Base Elevation (GLOBE) Digital Elevation Model, Version 1.0, Boulder, Colorado, USA, 1999.

Körner, C., Jetz, W., Paulsen, J., Payne, D., Rudmann-Maurer, K., and M. Spehn, E.: A global inventory of mountains for bio-geographical applications, Alp Bot, 127, https://doi.org/10.1007/s00035-016-0182-6, 2017.

Morlighem, M.: MEaSUREs BedMachine Antarctica, Version 2 , Boulder, Colorado USA. NASA National Snow and Ice Data Center Distributed Active Archive Center, https://doi.org/10.5067/E1QL9HFQ7A8M, 2020.

Morlighem, M., Williams, C. N., Rignot, E., An, L., Arndt, J. E., Bamber, J. L., Catania, G., Chauché, N., Dowdeswell, J. A., Dorschel, B., Fenty, I., Hogan, K., Howat, I., Hubbard, A., Jakobsson, M., Jordan, T. M., Kjeldsen, K. K., Millan, R., Mayer, L., Mouginot, J., Noël, B. P. Y., O'Cofaigh, C., Palmer, S., Rysgaard, S., Seroussi, H., Siegert, M. J., Slabon, P., Straneo, F., van den Broeke, M. R., Weinrebe, W., Wood, M., and Zinglersen, K. B.: BedMachine v3: Complete Bed Topography and Ocean Bathymetry Mapping of Greenland From Multibeam Echo Sounding Combined With Mass Conservation, Geophys Res Lett, 44, https://doi.org/10.1002/2017GL074954, 2017.

Morlighem, M., Rignot, E., Binder, T., Blankenship, D., Drews, R., Eagles, G., Eisen, O., Ferraccioli, F., Forsberg, R., Fretwell, P., Goel, V., Greenbaum, J. S., Gudmundsson, H., Guo, J., Helm, V., Hofstede, C., Howat, I., Humbert, A., Jokat, W., Karlsson, N. B., Lee, W. S., Matsuoka, K., Millan, R., Mouginot, J., Paden, J., Pattyn, F., Roberts, J., Rosier, S., Ruppel, A., Seroussi, H., Smith, E. C., Steinhage, D., Sun, B., Broeke, M. R. van den, Ommen, T. D. van, Wessem, M. van, and Young, D. A.: Deep glacial troughs and stabilizing ridges unveiled beneath the margins of the Antarctic ice sheet, Nat Geosci, 13, https://doi.org/10.1038/s41561-019-0510-8, 2020.

Morlighem, M., Williams, C. N., Rignot, E., An, L., Arndt, J. E., Bamber, J. L., Catania, G., Chauché, N., Dowdeswell, J. A., Dorschel, B., Fenty, I., Hogan, K., Howat, I., Hubbard, A., Jakobsson, M., Jordan, T. M., Kjeldsen, K. K., Millan, R., Mayer, L., Mouginot, J., Noël, B. P. Y., O'Cofaigh, C., Palmer, S., Rysgaard, S., Seroussi, H., Siegert, M. J., Slabon, P., Straneo, F., van den Broeke, M. R., Weinrebe, W., Wood, M., and Zinglersen, K. B.: IceBridge BedMachine Greenland, Version 4, Boulder, Colorado USA. NASA National Snow and Ice Data Center Distributed Active Archive Center, https://doi.org/10.5067/VLJ5YXKCNGXO, 2021.

Rastner, P., Bolch, T., Mölg, N., MacHguth, H., le Bris, R., and Paul, F.: The first complete inventory of the local glaciers and ice caps on Greenland, Cryosphere, 6, https://doi.org/10.5194/tc-6-1483-2012, 2012.
RGI-Consortium: Randolph Glacier Inventory - A Dataset of Global Glacier Outlines: Version 1.0, Boulder, Colorado, USA, https://doi.org/10.7265/p9yk-6m11, 2012.

RGI-Consortium: Randolph Glacier Inventory–A Dataset of Global Glacier Outlines: Version 6.0, Technical Report, Global Land Ice Measurements from Space, Colorado, USA, Boulder, Colorado, USA, https://doi.org/10.7265/4m1f-gd79, 2017.